UNIVERSITY OF CALIFORNIA, SAN DIEGO

Brake Rotor Design and Comparison using Finite Element Analysis: An Investigation in Topology Optimization

A thesis submitted in partial satisfaction of the
requirements for the degree
Master of Science

in

Engineering Sciences (Mechanical Engineering)

by

Kenneth Domond

Committee in charge:

Professor Frank E. Talke, Chair
Professor David J. Benson
Professor Nathan Delson

2010

The thesis of Kenneth Domond is approved and it is acceptable in quality and form for publication on microfilm and electronically:

_____

_____

_____
Chair

University of California, San Diego

2010

DEDICATION

Karl Domond
my younger brother and fellow engineer;

Junko and Oreste Domond
my parents;

Jaime Cortez
my motivation.

There is no man living that can not do more than he thinks he can.

—Henry Ford

TABLE OF CONTENTS

LIST OF FIGURES

LIST OF TABLES

ACKNOWLEDGEMENTS

I'd like to thank Professor Talke for his support, advise, guidance, and patience over the course of this effort. For the freedom to pursue this topic as well as the resources to conduct this work. Also, for a much better understanding of design and optimization methods from his instruction within and outside of his course work. Professor Delson for his advise, support, and suggestions on some topics that would help support my conclusions, and for his insight on industry practices. Professor Murakami for his expertise on the finite element method. I enjoyed the courses taken with you. Professor Benson for his expertise on the finite element method and advise on further expanding my knowledge to nonlinear finite element methods after graduation. Jaime Cortez, Jonathan Marquez, and all my other wonderful friends for their support and motivation. Without you guys enriching my life, the long nights would have been much longer. Zul, Mahesha, and others at Altair Engineering for their Hyperworks support and training. My parents, Junko and Oreste Domond, for their continued support and push to finish school sooner rather than later.

ABSTRACT OF THE THESIS

Brake Rotor Design and Comparison using Finite Element Analysis: An Investigation in Topology Optimization

by

Kenneth Domond

Master of Science in Engineering Sciences (Mechanical Engineering)

University of California San Diego, 2010

Professor Frank E. Talke, Chair

Disc brake technology used for mountain bikes, and mountain bike technology in general, has improved significantly as the sport of mountain biking has evolved. Disc brakes on bicycles are relatively new compared to their use on other vehicles. Rotor design is varied for rotors of the same intended use for many companies; some still use the same initial rotor designs that were introduced over a decade ago. Through the finite element analysis and optimization process, understanding the difficulties of designing disc brake rotors and the validity of certain design trends in current disc brake rotors is pursued. Additionally, this investigation uses finite element methods to design and optimize a mountain bike disc brake rotor using topology optimization. More specifically, the goal is to design a lighter rotor that maintains similar structural performance as rotors that are currently commercially available. The new rotor design was compared to two existing rotor geometries. The strength of the new rotor is comparable to existing rotors

A and B. Weight improvements of 14.3% and 12.4% over Rotor A and Rotor B, respectively, are realized.

Chapter 1

Introduction

With any design problem there are objectives and constraints that must be met. With mechanical design, size, weight, strength, and cost are a few of the many constraints that may need to be taken into consideration when designing for a set of objectives. Traditional methods of design rely on an engineer or a team of engineers' creativity, experience, and intuition to come up with several initial designs. These initial designs are compared and analyzed using simplified models, from which the best solution is chosen. The best design is then improved upon iteratively. These iterations are in essence cycles of trial and error that can often require many cycles, each of which can be costly and time consuming. With finite element analysis and optimization, more complex problems can be solved more quickly, decreasing the amount of physical testing for a new design. An optimum design can be achieved based on predetermined criteria using computational methods. Sometimes unforeseen problems arise and additional design goals need to be met; it is also possible to determine where and how changes should be made, if the intended use of the new product were to change, because all conditions for optimization are known. This helps address the cases where non-optimal designs may continue to be use to cut the time, cost, and risk of trying to find a better design. For these reasons, finite element techniques were chosen as the design method for designing a disc brake rotor.

Although disc brakes are not new, they have not been used on bicycles for

very long. Disc brakes for bicycles are most commonly seen on mountain bikes, because of how well they work in varying weather conditions, at high speeds, and under long braking periods. Mountain biking is a relatively new sport with influences originating from cyclocross[1] in Europe, Roughstuff Fellowship in the United Kingdom[5], and from gravity enthusiasts riding modified cruisers[2] down dirt trails in Marin County, California[6]. It began gaining mainstream popularity throughout the 1990s. Many ideas including disc brake design are still in the process of being perfected by engineers and hobbyists alike. There are a range of products and designs for almost every component of the mountain bike that are changing from year to year. These products are exhibited at various annual expos such as at the Interbike International Trade Expo[7] or the Sea Otter Classic Expo[8]. Marketing efforts and popularity trends often blur the line between real technological advances and product hype, and create situations where new technology may not be used where it is most applicable[3].

Disc brake technology has significantly influenced the limits of the mountain biking sport. In turn, disc brake technology has also been pushed by the evolving sport of mountain biking. Disc brakes on bicycles were not initially popular, because of the lack in stopping power of mechanical disc brakes compared to the standard rim brakes, and the reliability problems of early hydraulic systems. Now hydraulic systems are very robust, relatively light, and very easy to maintain. They include technologies that reduce brake fade more effectively and products

[1]Cyclocross is a type of race involving several laps on a course with various terrain including pavement grass, and wooded trails. Cyclocross bikes look like road bikes with knobby tires.

[2]Cruisers are bikes that allow a more upright and relaxed riding posture and usually have fatter tires than road bikes.

[3]A good example of this occurred around 2003 when mountain bike suspension design and damping technologies were still relatively simple. In a pioneering effort to introduce new damping technology to reduce pedal bobbing, many companies began making stable platform suspension systems. (Pedal bob is the vertical movement of the bike caused by pedaling. Stable platform suspension refers to suspension that contains some type of damping or valve system that keeps or helps keep the suspension from becoming too active under pedaling.) This was also around the time that long travel bikes used for more than just high speed gravity racing began gaining popularity; aggressive trail riding and extreme technical trail riding are more pedaling inclusive. This combination made long travel stable platform suspension a hit for a short period of time until riders began to realize that this decreased small bump sensitivity. This led to a large drop in stable platform fork and stable platform long travel rear shock popularity in subsequent years. It's primary presence remains in cross-country or short travel oriented suspension products.

that make maintaining the system much easier. Very recently hydraulic bicycle disc brakes with variable leverage ratios have been made that combine the advantages and reduce the disadvantages of previous systems,[4] making them even more desireable. Brake pad technology and brake fluid technology from other disc brake systems such as those on motorcycles have also trickled down into bicycle disc brake technology as the performance requirement became more demanding. However, even with the advancements in hydraulic actuation of disc brake systems, rotor design has remained relatively stagnant. Until recently, many companies used the same or similar rotor designs as when they introduced their first products. Hayes is an example of a company that has used a very similar rotor design for over a decade for all size rotors.

Performance due to differences in existing single alloy designs are not obvious. Many companies offer several rotors with different designs for similar applications. The designs also vary significantly from company to company. A few examples are shown in Figure A.4. Some companies are beginning to introduce rotors that use multiple alloys[5]. However, these rotors are much more expensive and take longer to make than steel rotors which are simply stamped, water jet cut, or laser cut out of steel sheets. Therefore finite element optimization techniques are used to design a single alloy disc brake rotor that is lighter and performs as well as existing single alloy rotors. The scope of this paper is to investigate rotor design using topological optimization for a single alloy disc brake rotor. All finite element analysis and optimization is done on a linear finite element solver, thus does not account for any cyclic loading or plastic deformations. Heat effects are also not considered. Although, plastic deformation and heat can affect the point of failure of a brake rotor, it is assumed that failure directly caused by these effects are not common. Under normal braking, the rotor should remain in its elastic region. Otherwise the rotor would deform after each use. Regarding failure by

[4]In earlier hydraulic disc brake systems leverage was not variable and forced two designs: the first option was more braking force and reduced piston travel, the second option was to have more piston travel to accommodate for bent rotors and mud with reduced braking force.

[5]Shimano is one of the pioneering companies that have experimented with multiple alloy designs in their proprietary Center Lock mounting system. They have used multi-alloy rotors since the mid 2000s.

overheating, brake system failure due to glazing of the brake pads or boiling of the brake fluid usually occur before rotor failure due to warping occurs. In addition, if heating becomes a problem under aggressive use, the traditional solution is to use a larger diameter rotor. Analysis is done to compare existing designs to a new design developed using Optistruct®, a finite element optimization software offered by Altair Engineering, Inc. The existing rotors chosen for comparison are a 160 mm Hayes rotor and a 160 mm Shimano rotor, here on referred to as Rotor A and Rotor B, respectively. Images of these rotors can be seen in Figure A.2 and A.3 in Appendix A.

Chapter 2

Disc Brake Overview

Disc brakes are a type of brake that uses discs (as opposed to rims or drums) as the braking surface. This type of brake is used on many types of vehicles such as cars, motorcycles, and bicycles. Their main advantages over other types of bicycle brakes are their ability to perform well in dry and wet conditions and under prolonged braking periods.

The main components of a disc brake system are the brake caliper, which houses pistons and brake pads, and the rotor. A typical configuration of disc brake caliper and rotor can be seen in the cross sectional view shown in Figure 2.1(a). Pistons are usually actuated hydraulically or mechanically, but can be actuated by other means such as pneumatics or electromagnetism as well. Bicycle disc brakes are almost exclusively actuated by hydraulic or mechanical means via a lever mounted to the handlebar. The hydraulic fluids most widely used are mineral oil, DOT 3, and DOT 4 fluids. Bicycle disc brakes are one of the few systems that still use mechanical means of actuation and do so with cables[1]. Although they are not typically as powerful as hydraulic disc brakes, their use is continued because they are generally cheaper and lighter. The user input is usually done via a hand lever. A cross section of a bicycle hydraulic lever can be seen in Figure 2.1(b).

On a bicycle, the rotor is mounted to the hub of the wheel. There are various proprietary mounting methods but a standard pattern of six T-25 screws is most widely used. The front disc brake caliper is typically mounted to the fork

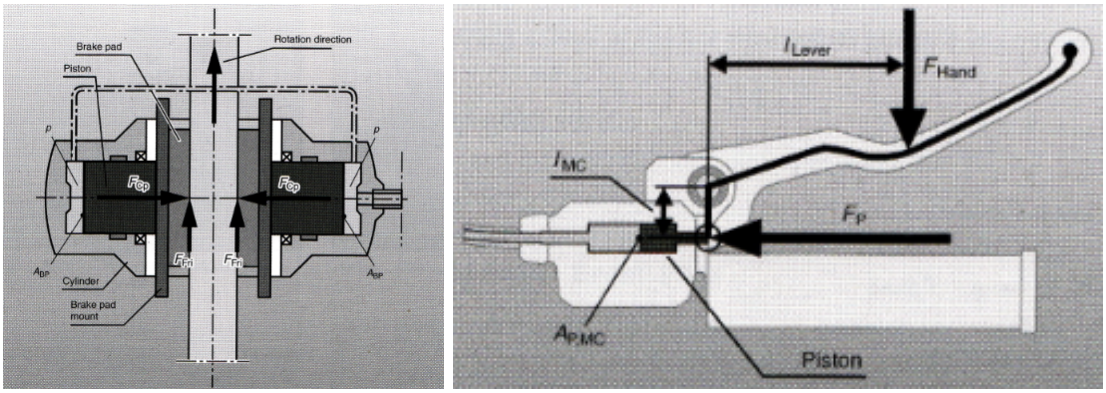

(a) (b)

Figure 2.1: Cross section of a disc brake caliper with brake pads in contact with a brake rotor (a) and hydraulic brake lever (b). Friction forces and pressure forces are also shown. Source:[1]

and the rear disc brake caliper is typically mounted to the seat stay of a bicycle. The lever is mounted to the handlebar. Figure 2.2 shows the mounting points for the front and rear disc brake system. The major parts of a bicycle are labeled in Figure A.1 in Appendix A.

Currently there are few regulations for bicycle disc brake performance except the general braking regulations for bicycles stated in Title 16 §1512.5 of the Code of Federal Regulations determined by the US Consumer Safety Commission[9]. These regulations offer a very large amount of freedom in brake design, limited primarily to distance before stopping and failure of the braking apparatus. For this reason the factor of safety for rotor failure can be as low as what is comfortable for each individual manufacture. Strength sufficiency of the newly designed rotor is based on comparisons to two existing rotors that have been in use for many years.

(a) front caliper and rotor

(b) rear caliper and rotor

(c) brake lever

Figure 2.2: How the disc brake system is typically mounted to a bicycle.

Chapter 3

Two Wheel Vehicle Dynamics

In addition to understanding how the braking system works, the physics behind braking on a bicycle must be examined in order to optimally design a rotor. Maximum forces on the rotor can be determined from examining bicycle stability under braking in a straight line. Examining the suspension dynamics shows how the reduction of rotor weight is will affect the performance of the bicycle.

3.1 Stability Under Braking

The following is an analysis on a fully rigid bicycle under braking. Equations 3.1, 3.2, and 3.3 give the force balance equations for Figure 3.1(a). The sum of forces in the x direction, and sum of moments about point G are dynamic equilibrium equations, because of the motion of the bicycle, and is set to the total mass of the system m_{sys} times the deceleration of the system a_{sys}, and $(ma)_{sys}$ times the height of m_{sys} from the ground, respectively. The sum of forces in the y direction is under static equilibrium, because there is no motion in the y direction, and can be set to zero.

$\sum F_x$:

$$f_1 + f_2 = (ma)_{sys} \tag{3.1}$$

$\sum F_y$:

$$N_1 + N_2 - W = 0 \tag{3.2}$$

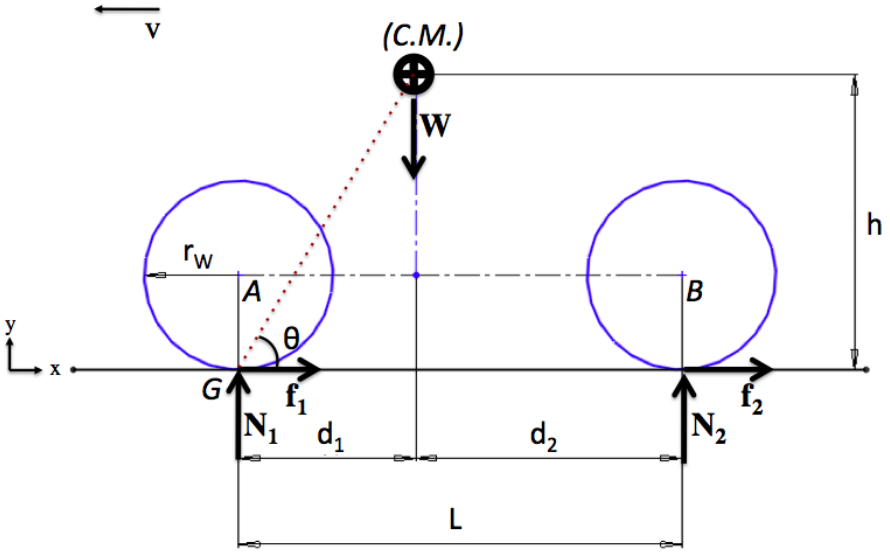

(a)

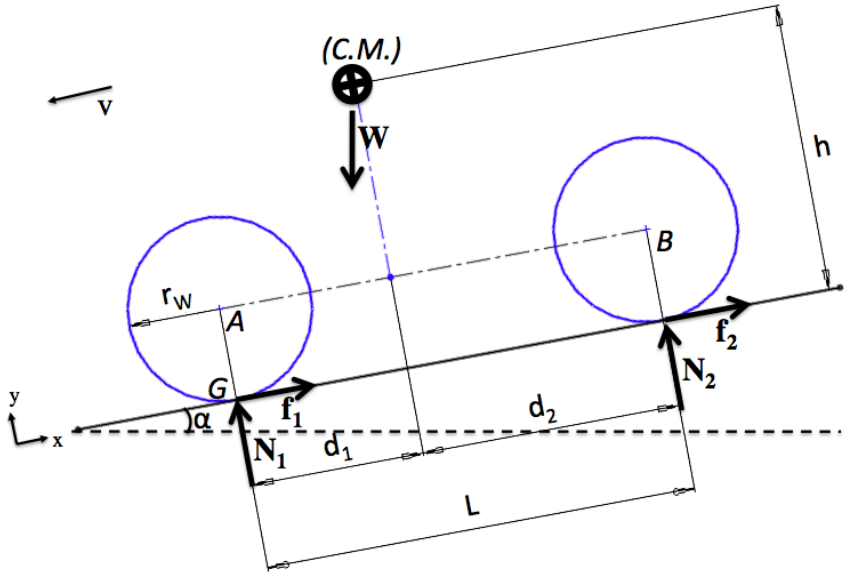

(b)

Figure 3.1: Free body diagram of a bicycle on (a) flat ground and (b) a slant.

$\sum M_G$:

$$-d_1W + LN_2 = -h(ma)_{sys} \tag{3.3}$$

N is the normal force, f is the friction force at the tire-road contact patch, and W is the combined weight of the rider and bicycle. Subscripts 1 and 2 indicate forces applied at the front and rear wheel, respectively. Coulomb friction f is defined as

$$f = \mu N, \tag{3.4}$$

where μ is the coefficient of friction. The subscript T indicates properties at the tire-road contact patch. Therefore, Equation 3.1 becomes

$$(ma)_{sys} = \mu_T(N_1 + N_2). \tag{3.5}$$

Plugging Equation 3.5 into Equation 3.3 leads to,

$$\begin{aligned} -d_1W + (d_1 + d_2)N_2 + h\mu_T(N_1 + N_2) = 0 \\ \Rightarrow -d_1W + LN_2 + h\mu_T N_1 + h\mu_T N_2 = 0 \\ \Rightarrow -d_1W + h\mu_T N_1 + (L + h\mu_T)N_2 = 0. \end{aligned}$$

Using Equation 3.2 this becomes,

$$\begin{aligned} -d_1W + h\mu_T N_1 + (L + h\mu_T)(W - N_1) = 0. \\ \Rightarrow -d_1W + LW - LN_1 + h\mu_T W = 0. \end{aligned}$$

Solving for N_1 gives,

$$N_1 = \tfrac{W}{-L}(d_1 - L - H\mu_T)$$

and simplifies to

$$N_1 = W\left(\frac{d_2 + h\mu_T}{L}\right). \tag{3.6}$$

Plugging back into Equation 3.2 gives,

$$N_2 = W\left(\frac{d_1 - h\mu_T}{L}\right). \tag{3.7}$$

Equation 3.7 is of particular interest because when $N_2 \leq 0$, the bicycle is no longer stable and means the rear wheel will lift; this is often called endoing. Instability or

the condition $N_2 \leq 0$ occurs when $\mu_T \geq \frac{d_1}{h}$. The variables d_1 and h are dimensions that locate the center of mass for the combined rider and bike mass relative to point G when the instability condition $\mu_T \geq \frac{d_1}{h}$ occurs. A line can be drawn from point G to the center of mass at position (d_1, h), which creates an angle θ with the ground. Angle θ can be defined as

$$\theta = \tan^{-1}\left(\frac{h}{d_1}\right), \tag{3.8}$$

or,

$$\theta = \tan^{-1}\left(\frac{1}{\mu_T}\right). \tag{3.9}$$

This line is a stability boundary that the combined center of mass of the rider and bicycle must remain behind for the bicycle to remain stable in the forward-aft direction[1]. This only holds true if the wheels are locked (i.e. no wheel rotation).

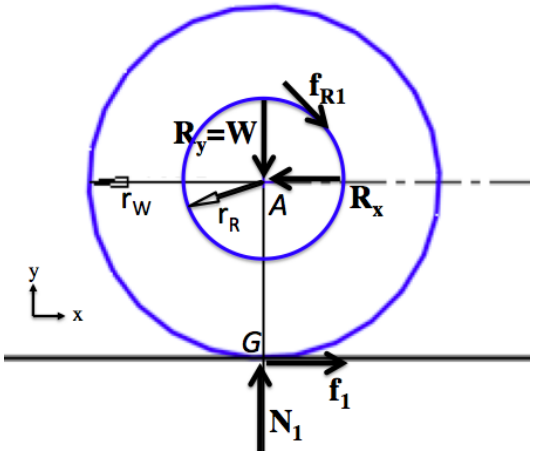

Figure 3.2: Free body diagram of a bicycle's front wheel at the instance of instability.

To understand when the wheels will be locked, force balances on the wheel must be looked at (see Figure 3.2). Because the wheel does not move in the x or y direction relative to the bike fork or frame only the moment equation is shown:

[1]Unless the rider is skilled enough to sufficiently lower his center of gravity, the rear wheel can expect to lift at deceleration rates over approximately .5 G or 4.9 m/s^2[10][11].

$\sum M_A$:

$$-r_R f_{R1} + r_W f_1 = 0, \tag{3.10}$$

where r is the radius of the rotor or wheel denoted by subscripts R and W, respectively. Using Equation 3.4 Equation 3.10 becomes,

$$-r_R \mu_R n N_P + r_W \mu_T N_1 = 0, \tag{3.11}$$

where μ_R is the coefficient of friction between brake rotor and pad, N_P is the normal force of the piston on the rotor, and n is the number of pistons acting on the rotor. Solving for μ_T gives,

$$\mu_T = \frac{r_R \mu_R n N_P}{r_W N_1}. \tag{3.12}$$

So,

$$\mu_T \leq \frac{r_R \mu_R n N_P}{r_W N_1}, \tag{3.13}$$

for the front wheel to remain locked.

In the case that the wheel is not locked instability can still occur. By plugging Equation 3.12 into Equations 3.7 and 3.9 it is seen that instability occurs when $\mu_R \geq \frac{d_1 r_W N_1}{h r_R n N_P}$, and the instability boundary can be drawn by

$$\theta = \tan^{-1}\left(\frac{r_W N_1}{r_R \mu_R n N_P}\right) \tag{3.14}$$

for $N_1 > 0$. These equations are useful because the pad and rotor contact area will always experience kinetic friction when applying the brakes under motion.

Another equation of interest arrises from Equations 3.2 and 3.3:

$$-\left(\frac{d_1}{h m_{sys}}\right) N_1 + \left(\frac{d_2}{h m_{sys}}\right) N_2 = -a_{sys}. \tag{3.15}$$

Equation 3.15 shows that as a_{sys} increase (e.g. higher decelerations) N_1 increases and N_2 decreases. In cases where the bike is not on flat ground as shown in Figure 3.1(b), there is an x component of the weight vector making Equation 3.15:

$$-\left(\frac{d_1}{h m_{sys}}\right) N_1 + \left(\frac{d_2}{h m_{sys}}\right) N_2 + h m_{sys} W \sin\alpha = -a_{sys}. \tag{3.16}$$

Equation 3.16 shows that the deceleration greatest when $N_2 = 0$ and when $\alpha = 0$ for $90 \geq \alpha \geq 0$. The term $hm_{sys} \sin \alpha W$ is a moment caused by a gravitational force, so even though it is negative when $0 > \alpha \geq -90$ and contributes to higher deceleration, the deceleration forces due to braking do not increase.

The above cases all assume the tire-road contact is great enough to cause instability whether skidding is present or not. On asphalt, the limiting factor of deceleration is bicycle stability rather than the tire-road friction coefficient[11]. Also, static friction is greater than kinetic friction. Therefore, maximum deceleration due to braking forces is seen at the instance before the bike becomes unstable on flat ground with no skidding. Because stresses on the brake rotors increase as braking forces increase and all loads are at the front wheel during maximum deceleration, maximum stresses seen by a rotor are on the front rotor at the instance before the bicycle becomes unstable. These conclusions apply to full suspension bikes as well. Even if brake dive and brake squat are taken into consideration, the dimensions locating the center of mass simply become time dependent (e.g. h, d_1, and d_2 become $h(t)$, $d_1(t)$, and $d_2(t)$, respectively) and the same method will give the same conclusions. In general the main effects of brake dive are the forward and downward shift of the center of mass due to the fork compressing under braking. Brake squat occurs in some full suspension bikes where the braking moments from the rear wheel cause the the rear suspension to compress; the result is the rearward and downward shift of the center of mass. Additional circumstantial cases where the normal forces are larger due to dropping from a point above the ground or from changes in the grounds slope over time are not considered.

3.2 Effects of Reduced Mass

There are many advantages for reducing the mass of a vehicle, and on a bicycle in particular. The most apparent reason is that it takes less work to lift a less massive object. This is more important for competitive endurance racing bikes, such as cross-country mountain bikes or road bikes where there is a significant amout of climbing and every gram matters. It is also easier to change the direction

of a less massive bike. This is a desirable trait in bikes ridden on trails with many turns or those used for tricks while jumping. The reduction in mass of a rotor is a small percentage of the total rider and bike mass, but it is a collection of components that make up the total mass of the bike. While reducing the mass of the rotor alone may seem insignificant, doing so along with mass reductions of all other possible components can be significant. In addition, the reasons for reducing rotor weight becomes more significant on a fully suspended bicycle; that is, a bicycle with independent suspension for the front and rear wheel. Just as it is easier to change the direction of a bike with less mass, it is easier to change the direction of a wheel with less mass. Reducing the mass of a rotor is one step to making a less massive wheel.

How well the wheel tracks the ground is very important especially for competitive gravity mountain biking events, where the fastest rider to the bottom of the mountain wins. These courses are often very technical with many natural and man made obstacles, often requiring high speed turns and hard braking. The more time the wheel can stay in contact with the ground, the more traction the rider will have. Therefore reducing unsprung mass should be a priority in performance mountain bike design.

Most vertical motion of a bicycle is caused by the contour of the ground. This motion also tends to be of relative high frequency on dirt trails where rocks and roots are abundant. For a full suspension bicycle only the parts that are below the springs and dampers, the unsprung components, see most of the high frequency motions.

A simplified model of a full suspension bicycle is a three mass, two spring, and two damper system with four degrees of freedom shown in Figure 3.3.

Forces exerted by springs and dampers are shown by Equations 3.17 and 3.18, respectively:

$$F = -kx, \tag{3.17}$$

$$F = -c\dot{x}, \tag{3.18}$$

where k is the spring constant, c and the damping constant, and the symbol $\dot{}$ is $\frac{d}{dt}$.

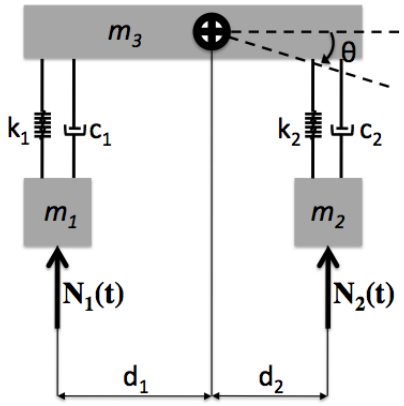

Figure 3.3: A full suspension bicycle modeled as a 4 degree of freedom mass, spring, damper system.

The general form of a damped mass-spring system is given in Equation 3.19:

$$\mathbf{M}\ddot{\mathbf{x}} + \mathbf{C}\dot{\mathbf{x}} + \mathbf{K}\mathbf{x} = \mathbf{F}(t), \tag{3.19}$$

where $\mathbf{M}$ is the mass matrix, $\mathbf{C}$ is the damping matrix, and $\mathbf{K}$ is the stiffness matrix. The variables $\ddot{\mathbf{x}}$, $\dot{\mathbf{x}}$, $\mathbf{x}$, and $\mathbf{F}$ are column vectors.

By performing a force balance, the model in Figure 3.3 can be represented by four equations:

$$\begin{aligned} m_3\ddot{x}_3 + k_1(x_3 - x_1 - d_1\theta) + c_1(\dot{x}_3 - \dot{x}_1 - d_1\dot{\theta}) \\ + k_2(x_3 - x_2 + d_2\theta) + c_2(\dot{x}_3 - \dot{x}_2 + d_2\dot{\theta}) &= 0 \end{aligned} \tag{3.20}$$

$$\begin{aligned} J_3\ddot{\theta}_3 - k_1(x_3 - x_1 - d_1\theta)d_1 - c_1(\dot{x}_3 - \dot{x}_1 - d_1\dot{\theta})d_1 \\ + k_2(x_3 - x_2 + d_2\theta)d_2 + c_2(\dot{x}_3 - \dot{x}_2 + d_2\dot{\theta})d_2 &= 0 \end{aligned} \tag{3.21}$$

$$m_1\ddot{x}_1 + k_1(x_1 - x_3 + d_1\theta) + c_1(\dot{x}_1 - \dot{x}_3 + d_1\dot{\theta}) = N_1(t) \tag{3.22}$$

$$m_2\ddot{x}_2 + k_2(x_2 - x_3 - d_2\theta) + c_2(\dot{x}_2 - \dot{x}_3 - d_2\dot{\theta}) = N_2(t) \tag{3.23}$$

Equations 3.20 through 3.23 are represented in the general matrix form:

$$\begin{bmatrix} m_1 & 0 & 0 & 0 \\ 0 & m_2 & 0 & 0 \\ 0 & 0 & m_3 & 0 \\ 0 & 0 & 0 & J_3 \end{bmatrix} \begin{Bmatrix} \ddot{x}_1 \\ \ddot{x}_2 \\ \ddot{x}_3 \\ \ddot{\theta} \end{Bmatrix} + \begin{bmatrix} c_1 & 0 & -c_1 & c_1 d_1 \\ 0 & c_2 & -c_2 & -c_2 d_2 \\ -c_1 & -c_2 & c_1 + c_2 & -c_1 d_1 + c_2 d_2 \\ c_1 d_1 & -c_2 d_2 & -c_1 d_1 + c_2 d_2 & c_1 d_1^2 + c_2 d_2^2 \end{bmatrix} \begin{Bmatrix} \dot{x}_1 \\ \dot{x}_2 \\ \dot{x}_3 \\ \dot{\theta} \end{Bmatrix} + \begin{bmatrix} k_1 & 0 & -k_1 & k_1 d_1 \\ 0 & k_2 & -k_2 & -k_2 d_2 \\ -k_1 & -k_2 & k_1 + k_2 & -k_1 d_1 + k_2 d_2 \\ k_1 d_1 & -k_2 d_2 & -k_1 d_1 + k_2 d_2 & k_1 d_1^2 + k_2 d_2^2 \end{bmatrix} \begin{Bmatrix} x_1 \\ x_2 \\ x_3 \\ \theta \end{Bmatrix} = \begin{Bmatrix} N_1(t) \\ N_2(t) \\ 0 \\ 0 \end{Bmatrix} \tag{3.24}$$

$N_1(t)$ and $N_2(t)$ are functions that represent the normal force at the front and rear wheel at time t. The sprung weight, m_3, usually consists of the rider, bicycle frame without the swingarm, seat, handlebar and controls, and upper fork.[2] The front unsprung weight, m_1, usually consists of a wheel, tire, brake rotor, brake caliper, and fork lowers. The rear unsprung weight, m_2, usually consists of a wheel, tire, sprocket, rear derailleur, brake rotor, brake caliper, swingarm, and some chain mass. Reducing the weight of the rotors will decrease the unsprung weight. It is not explicit, but with known values, Equation 3.24 will show that as m_1 and m_2 approach 0, the time the tires are in contact with the ground (where $N \geq 0$) increases. More generally, as the unsprung mass is decreased, the ability to change its direction increases. This means the wheels can track higher frequency perturbations at the ground, equivalent to increased control.

Reducing rotor weight also reduces the rotational mass of the wheels. This helps with forward acceleration of the bicycle. Rotational mass can be compared

[2] A labelled diagram of bicycle components can be found in Figure A.1 in the Appendix.

to equivalent mass moving in a linear path with the kinetic energy equation

$$KE = \frac{1}{2}mv^2 + \frac{1}{2}J\omega^2 = \frac{1}{2}m_{eq}v^2, \tag{3.25}$$

where v is velocity and ω is angular velocity.

Chapter 4

Finite Element Optimization Overview

4.1 Finite Element Method

Finite element analysis or the finite element method is a type of computational analysis use to solve a system of differential equations (DE) that have a set of restraints or boundary conditions (BC). These differential equations are also called boundary value problems (BVP). BVPs can be represented in their strong or classical form, and their weak or variational form. The strong form is simply a DE and its BCs stated explicitly. The weak form is equivalent to the strong form but consists of trial solutions, and weighting functions (also known as variations). In mechanics, equations in this form are often called equations of virtual work. The finite element method finds approximate solutions for BVPs from the weak form. For further explanation of strong and weak forms and their equivalence can be found in Hughes[12].

Computational analysis requires that the region, Ω, governed by the differential equation be discretized into subregions, Ω^e, called elements; solving for the infinite points within Ω is impractical. The elements collectively are called a mesh. Points where more than 2 elements share a boundary is called a node. Because of the discretization, only an approximation of the solution can be found for a

given BVP. How close the approximation is to the actual solution depends on how finely the region governed by the differential equation is discretized. The finer the discretization the closer the results will be to the actual solution. However, this comes at the cost of more computations and thus requires more computing power or time. To deal with this problem finer elements are used in regions of importance and larger ones in areas that hold less interest or significance.

The solution can be more reliable if higher quality elements are used as well. The more skewed an element is the less accurate the solution[13].

Element shape can vary as well. Trias and quad elements are common 2-D elements. Hexa, penta, tetra, and pyramid elements are common 3-D elements. The choice of element depends on the problem being analyzed, the accuracy needed, and the computational resources available.

For example, generally 2-D or shell elements are computationally less costly than 3-D elements because there are usually fewer nodes per element[1]. However, 2-D elements only allow a good representation of flat and thin objects with uniform thickness. Also, if using 2-D elements for thin objects moving out of plane of the 2-D element, in the third dimension, the elements become referred to as plate elements. Although plate and shell elements are both 2-D elements and look the same in a mesh the equations relating the elements together to arrive at a solution are very different. Most of the plate elements used in FEA is based on Reissner-Mindlin Theory. C^0 plate elements should generally not be used because of the tendency for shear locking; shear locking is when the model solution is stiffer than it should be. The problems of shear locking in Reissner-Mindlin plate theory is briefly discussed in Hughes[12] and is a well know problem that has led to the birth of plate elements other than the basic C^0 element. It is things like this that make the choice of element important in certain FE models. Recommendations for 2-D elements used as plate elements is provided by Altair[2].

There are many methods for solving boundary value problems but a common method in finite element analysis is the Bubnov-Galerkin Method widely know

[1]There are elements with nodes at places other than their vertices

simply as the Galerkin Method. The Galerkin Equation in matrix form

$$\mathbf{Kd} = \mathbf{F} \tag{4.1}$$

is the differential equation to be solved for static loading cases. The solution is

$$\mathbf{d} = \mathbf{K}^{-1}\mathbf{F} \tag{4.2}$$

and is often non-trivial to achieve. $\mathbf{K}$ is the global stiffness matrix, and defines the properties and element relations of the mesh; $\mathbf{d}$ is the displacement vector, containing the displacement of each node; $\mathbf{F}$ is the force vector. The global stiffness matrix is formulated from elemental stiffness matrices, $\mathbf{k}^e$, which is formulated from the bulk modulus, $\mathbf{B}$, and material modulus matrix, $\mathbf{D}$:

$$\mathbf{k}^e = \int_{\Omega^e} \mathbf{B}^T\mathbf{D}\mathbf{B}d\Omega \tag{4.3}$$

The material modulus matrix contains shear and normal stiffness coefficient for the material applied to the region Ω. The bulk modulus is a matrix of basis or shape functions for an element. What shape function is used depends on the order of the differential equation. For higher order differential equations smoother shape functions are required. For example, piecewise quadratic shape functions that are C^1 functions are needed for 4th order differential equations[12]. The strain tensor, ϵ, can be calculated once the displacements are found:

$$\epsilon_{ij} = \frac{\partial_j \mathbf{d}_i + \partial_i \mathbf{d}_j}{2} \tag{4.4}$$

The stress can subsequently be found using Hooke's Law:

$$\sigma = \mathbf{C}\epsilon \tag{4.5}$$

$\mathbf{C}$ is the material elasticity matrix and σ is the stress tensor.

Linear buckling analysis using the finite element method is also possible. Buckling loads can be calculated by solving the eigenvalue problem:

$$[\mathbf{K} - \lambda\mathbf{K_G}]\mathbf{x} = \mathbf{0} \tag{4.6}$$

using the Lanzcos Method, where $\mathbf{K}$ is the material stiffness matrix, $\mathbf{K_G}$ geometric stiffness matrix, $\mathbf{x}$ is the eigenvector for the eigenvalue λ.

4.2 Optimization Overview

Designing a product to solve a specific problem can be very time consuming and complicated. Often, multiple designs can solve the same problem, but one may perform more favorably in one area and not so favorably in another. Although testing is essential to prove a design, using trial and error is a very expensive and time consuming method to optimize a design. This method also becomes very difficult when several design variables and constraints are present. Alternate optimization methods have been developed to address such difficult optimization problems. Most methods use a cost function, which is a function that includes and relates all important variables within a problem with the optimization goal. Minimizing or maximizing the cost function will lead to a solution that is the design that contains the optimal parameters for its defined variables. Design constraints are also applied to the cost function to ensure that the optimum solution does not lie outside the acceptable range of design parameters. In other words, the best solution within the constraint boundaries will be found. If a cost function only contains a few variables it is sometimes possible to minimize (or maximize) it analytically. However, for those that are too complex to solve analytically, many computational methods exist.

An optimization problem can be expressed mathematically with a cost function E. This cost function should include all considered design variables and their relationship to the optimization goal (i.e., if weight of a beam is the optimization response in question, simply using the radius of a beam is not sufficient; the relationship between the radius and weight need to be used). Thus,

$$E = f(\mathbf{D}), \tag{4.7}$$

where $\mathbf{D}$ is a vector containing all design variables to be considered. The cost function can also be subject to equality constraints,

$$g(\mathbf{D}) = 0 \tag{4.8}$$

and inequality constraints,

$$g(\mathbf{D}) \leq 0, \tag{4.9}$$

$$g(\mathbf{D}) \geq 0. \tag{4.10}$$

The amount of influence of each variable in the final design can also be included by weighting parts of the cost function[14].

4.3 Optistruct

Optistruct is a linear solver developed by Altair Engineering. Optistruct can find solutions for linear static analysis, normal modes analysis, linear buckling analysis, and frequency response analysis using the modal method.

There are a few nonlinear problems that Optistruct can solve using iterative methods. Optistruct can solve quasi-static problems using Newton's Method[2]. Quasi-static solutions are a series of static solutions found over some discrete intervals of time. This is useful for problems where the boundary conditions are not constant over time. Because the of the quasi-static requirement for Optistruct, the behavior of the loads and constraints over time must be known before analysis. Therefore, transient response analysis is not possible. Any analysis that requires non-linear relationships between nodes, such as fluid, heat, or fatigue analysis, is not supported.

Solutions can only be found where a mesh is present. In situations where there are spaces or gaps in the mesh where contact with another part of a mesh is possible, gap elements can be used. Gap elements are elements with very little stiffness, simulating lack of connectivity, until a threshold is reached. At this threshold the stiffness becomes very high, simulating contact. This allows analysis of bodies that may collide with each other. The gap element's properties change relative to distance of the two nodes it connects. Figure 4.1 shows the relationship of distance and the gap elements' stiffness in Optistruct. In the case where contact is simulated the force the gap element exerts on the mesh is determined by the distance the nodes pass each other via a penalty method[2][14]. The greater the distance between the nodes past the threshold point, the greater the penalty or force in the opposite direction the nodes are traveling. The distance between nodes at the point impact is simulated is the threshold where the gap elements switch

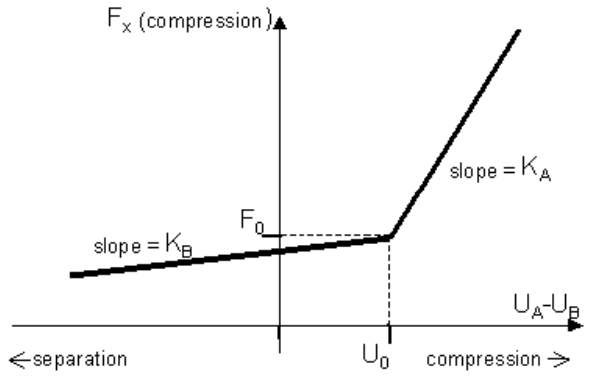

Figure 4.1: Non-linear force deflection curve of Optistruct CGAP elements, before and after threshold U_0. K is the stiffness of the gap element. $U_A - U_B$ is the size of the opening. Source: [2]

from one set of properties to the other, however, this threshold can be set to any desired distance. The forces the gap elements exert on the mesh are calculated iteratively.

Optimization in Optistruct uses the direct method and the adjoint variable method; the chosen method is determined automatically by Optistruct.

The direct algorithm is an acronym for DIviding RECTangles. This method is called such because of the partitioning of the search space into hyper-rectangles to find an optimal hyper-rectangle. The function being optimized is normalized to fit an n-dimensional unit hyper-cube. Once the search space is partitioned the cost function is evaluated at the center point of each partitioned area. The hyper-rectangle with the lowest evaluated center point is the optimal hyper-rectangle and becomes the new search space. This hyper-rectangle is partitioned and the process is repeated until the global minimum to some determined resolution is found. Figure 4.2 is an example of the direct method process on a two dimensional search space. The dots in Figures 4.2 show the function evaluated at each center point. The unfilled dot represents the lowest calculated value. The shaded area is the portion of the search space being considered at that particular iteration. Further explanation of the direct method can be found in Zhu et. al.[3].

The adjoint variable method is a gradient-based optimization method that

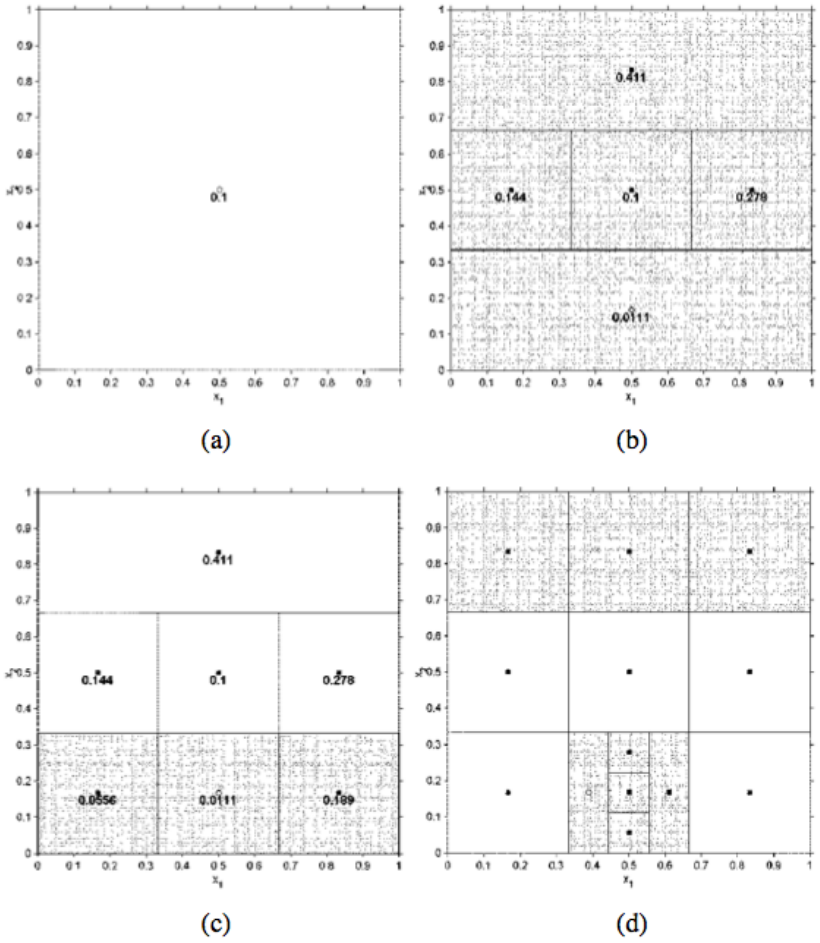

Figure 4.2: Direct Method performed through 4 subsequent iterations shown (a)-(d) respectively. The unfilled dot represents the rectangle with the lowest value. Source: [3]

uses adjoint equations to determine search vectors towards the minimum or maximum of a cost function. Other types of gradient-based optimization methods include the steepest descent method and the conjugate gradient method. The only difference between these is how the gradient and direction vector is solved for, when moving towards minima or maxima. Further explanations of the adjoint variable method can be found in Sergeant[15]. Further explanations of the steepest descent method and the conjugate gradient method can be found in Shewchuck[16]. The OptiStruct topology optimization solves structural optimization problems where the cost function is determined by the finite element model and optimization objective, and the constraint functions are user defined constraints entered into Hypermesh.

These and additional details on Optistruct and its capabilites can be found in the Optistruct Help Manual[2].

Chapter 5

Pre-Processing

5.1 Modeling

In order to optimize a design, the actual system must be well understood; then a sufficient model of the real system can be created. This includes understanding the forces and constraints on the system, the materials of the system, and the geometry of the system under consideration.

5.1.1 Load Modelling

Boundary conditions (BC) are the loads and constraints acting on a particular mesh. To know what BC to implement on the mesh of the rotor, actual forces on a rotor in use must be determined. Proper BCs are those that represent actual forces accurately enough for the results to be of any significance. §3.1 examines the affects of braking on the rotor. Although the analysis in §3.1 shows the relationship between multiple bodied under braking it is still necessary to replace variables with specific values in order to determine a satisfactory explicit value for the BC loads and constraints. Much of the information needed for a reasonable model under all braking conditions for various riders is not realistic, mainly because it would lead to an infinite combinations of BC and infinite cases for analysis. Fortunately, only the worst case under most circumstances is needed to ensure that failure is very improbable for the new rotor design under normal use.

Most adult males are less massive than 100 kg based on US National Health and Nutrition Exam Survey 99-02 [17] and Hermanussen [18]. This value was used as a general reference for human body mass. Bicycle weight varies greatly from very light performance road bikes to very heavy down hill mountain bikes meant for heavy abuse. A mass of 15 kg was used for the bicycle. Although heavier bikes exist they typically are used for more gravity oriented riding styles which typically use larger rotors[1]. Combined, a total rider and bike mass of 115 kg was used. For the highest loads on the rotor due to braking, as discussed in §3.1, 100% of this weight is on the front wheel. Therefore, the normal force N is 1128 N. Also see Figure 3.2 for a free body diagram of a bicycle's front wheel under braking. When a wheel is rolling no relative motion occurs between the tire and the ground at the contact interface so static friction can be used; the same applies to braking without skidding [19]. This is not to be confused with rolling resistance, which does not use a dimensionless coefficient and is related to the adhesion and deformation interactions[2] between the wheel and ground [20]. The static friction coefficient is about .9 for rubber on asphalt [21]. Using Coulomb friction (Equation 3.4), the maximum friction force the front tire-asphalt contact patch f_1 can see under braking is 1015 N. The standard mountain bike wheel diameter is .6604 m (26 in), so the moment caused by f_1 about the axle or center of the wheel point A would be 335 Nm. Under dynamic equilibrium the moment caused by f_1 must equal the moment caused by the friction force of the rotor-pad contact patch f_{R1} about point A (Equation 3.10). For a 160 mm rotor[3], f_{R1} would be about 4200 N.

The calculated value for the friction force of the brake pad exerted on the rotor is a very approximate value based on values chosen from the statistical cases

[1]Larger rotors provide increased braking power and greater surface area for heat dissipation. Generally, if a rotor is not powerful enough or is overheating too often for the riding style, larger rotors are used [1]. For this reason, effects on heat dissipation due to reduced surface area is not considered.

[2]Forces form rolling resistance vary greatly depending on tire thickness, air pressure, wheel diameter, and surface contours of the tire and ground. However, they are small relative to other forces and have been neglected in these calculations.

[3]"Eight inch"(203 mm) and "six inch"(160mm) rotors are the most commonly used rotor diameters, although "seven inch"(185mm) and 140mm rotors are becoming popular as well. Rotor size used for optimization was the 160 mm rotor.

and assumed values mentioned in the previous paragraph. However, it coincides closely with the maximum recommended torque for a Hayes rotor. The published value is approximately 312 Nm (230 ft-lbs), which is about 3900 N at 80 mm [22]. A value near both the calculated friction force and the friction force resultant of the Hayes data was used; the value for the friction force at the pad-rotor interface used for the finite element model was 4000N. The strength of the new rotor design is compared to the strength of existing designs under the same BCs, to provide a reference point to aid in validation, in case the approximated friction force of 4000N is too high or too low of an estimate.

Analytically solving for the friction force, rather than model the pad-rotor interface using normal forces and friction coefficients, was done because theoretically any amount of normal force could be applied to the rotor regardless of the strength of a human finger. This normal force depends on the ratios between the actuator piston size and the caliper piston size. Solving for the friction force analytically allows for a maximum friction force at the rotor that is limited by tire-road friction rather than the braking strength.

5.1.2 Meshing

Hypermesh automatically generates a mesh from geometry [23]. The geometry can be created within Hypermesh itself, or imported from a number of Computer Aided Design (CAD) software. Rotor geometry was created in Solidworks and imported into Hypermesh as an Initial Graphics Exchange Specification (IGES) file. The mesh was auto-generated using approximately 1 mm sized trias shell elements with some curvature and proximity biasing to increase mesh density where edge curvature is small or edges are close in proximity. The 1 mm size was chosen to ensure that geometrical features of at least 1 mm would show up in optimization solutions. The selection of trias elements over quad elements was arbitrary. They are both solved similarly using the Galerkin Method if all loads and displacements are all in the same 2 dimensional plane as the elements themselves. Each element was assigned to be 1.75 mm in thickness with the material

properties given in §§5.1.5; rotors are typically 1.75 mm thick.

Gap elements were given stiffness properties based on the stiffness of their surrounding elements. Of course this stiffness is applied only during simulated contact situations where the gap element exerts a force opposing mesh overlap. The iterations for non-linear loading was limited to 25 (see §4.3). Gap elements must be associated with a coordinate system in order to define its orientation (e.g. the overlap direction mush be defined). Cylindrical coordinate systems were created, each with its origin at the center of each bolt hole. Gap elements connecting the bolts to the rotor were assigned to respective coordinated systems.

Every disc for analysis has to be meshed. This includes existing rotors A and B during initial analyses, the generic rotor for optimization, and all subsequently analyzed rotors developed from optimization solutions. The generic rotor refers to a blank rotor, without any design features, that is used for topology optimization; it is essential a solid disc that can be mounted to the standard 6 bolt mount on a bicycle hub (see Figure 5.6).

Rotor A consists of 22,552 trais elements, 6 rigid elements, and 72,906 total degrees of freedom (DOF). Rotor B consists of 22,049 trias elements, 6 rigid elements, and 72,396 total DOF. The generic disc consists of 35,386 trias elements, 6 rigid elements, and 108,234 total DOF. When bolts were modeled with gap elements the generic disc had 35,386 trias elements, 6 rigid elements, 96 gap elements, and 109,188 total DOF. The newly designed disc after optimization and result interpretation consisted of 20,400 trias elements, 6 rigid elements, and 68,244 total DOF. See §§5.1.3 for how screws were modeled for various mounting conditions.

5.1.3 Boundary Conditions

Boundary conditions (BC) are the loads and constraints acting on a particular mesh. In FEA exact representation of loads on a system cannot be modeled and must be represented discretely for the same reasons a body must be discretized into elements.

Loads

In §§5.1.1 it was determined that 4000 N was a reasonable estimation for the maximum friction forces on a rotor due to braking. This friction force occurs at the pad-rotor interface. In hydraulic disc brakes the pad is pressed to the rotor by a floating piston, so the load on the rotor from the pad is fairly uniform (see Figure 2.1(a). Thus, in the FE model, the load was distributed uniformly across nodes on the rotor's braking surface that intersected the brake pad area, shown in Figure 5.1.

Loads can be modeled several ways often with similar results. Just as a distributed load can be represented with a single equivalent point load in conventional statics and dynamic analysis, a distributed load can be modeled as several small point loads distributed over multiple nodes or as one large equivalent load on one node (see Figure 5.2).

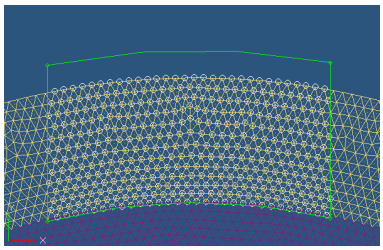

Figure 5.1: Nodes on the rotor's braking surface that coincide with the brake pad's contact area.

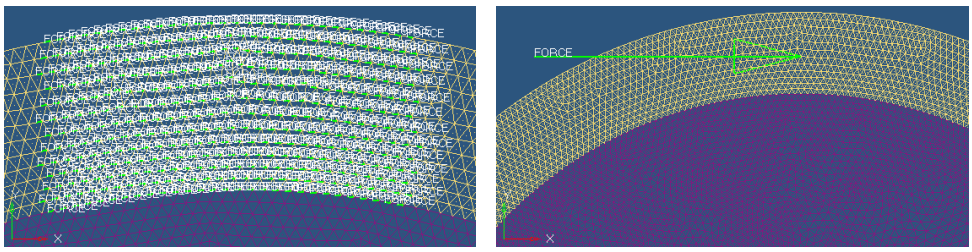

(a) (b)

Figure 5.2: Equivalent distributed (a) and point (b) loads on the rotor's mesh.

This is demonstrated by comparing analysis results of Rotor B under equivalent distributed and point loads shown in Figure C.1 in Appendix C. Note the large localized stresses around the point load in Figure C.1(a) and the similar stress distribution to that of Figure C.1(b) in areas further from the load. Point loads were often used in place of distributed loads to decrease pre-processing setup time because of the number of model cases processed, but were verified using distributed loads once satisfactory models were found. All optimization was done using distributed loads although similar results were also attained using point loads.

While the rotor rotates, there are infinite positions around the circumference of the rotor where the pads can be when braking occurs. Although it is desirable to ensure that the rotor is optimized for all rotational orientations, this is not possible; in a linear finite element model it is not possible to move the loads relative to the mesh over time as the pads would move about a real rotor. Fortunately, because of the cyclic symmetry most of the orientations are redundant. Two pad placements about the rotor were chosen to simulate two of the rotor's rotational orientations; a load case was created for each of the rotor's cyclic symmetry configurations. The first position is with the pad radially inline with a bolt. The second positions is with the pad equally spaced between two bolts. There are six bolt holes, thus through symmetry these two positions cover 12 positions about the rotor. Figure 5.3 shows the two cases of symmetry and the two load cases for the generic rotor to be optimized.

Each load case is considered simultaneously during optimization, but having multiple load cases on a single model is not the same as having both load cases applied to the rotor at the same time. Each position provides slightly different optimization solutions as seen by comparing Figures C.2(a) and C.2(b). All other possible solutions from pad positions between pad positions in load cases 1 and 2 should be some combination of these two solutions. It is assumed that simultaneously considering just the two orientations on the cyclic planes is sufficient for an optimization design that is good for all orientations. A compromised solution resultant from simultaneously solving for both load cases is shown in Figure C.2(c).

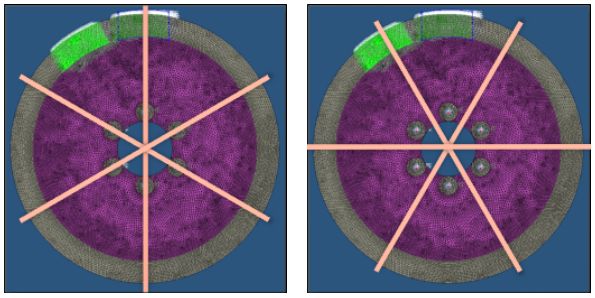

(a) Load Case 1: Aligned with bolt holes.

(b) Load Case 2: Unaligned with bolt holes.

Figure 5.3: Two cases of cyclic symmetry for the generic

Physical Constraints

The rotor is mounted to the hub of the wheel by six T-25 screws in a standardized six hole pattern. Although torque specifications for mounting the rotor to the hub exist, many bicycle owners do not own the tools to correctly do so. Even if the rotor is mounted correctly, it is possible for the screws to become loose over time. Therefore, several mounting cases must be considered:

Case 1: the screws are loose with no shear or friction restraint by the screw head (i.e. the rotor can wiggle around freely due to the tolerances between the clearance hole and screw threads, but cannot rotate with respect to the wheel).

Case 2: the screws are fully tightened and the rotor is fully constrained to the wheel.

Case 3: the screws are somewhere between fully tightened and fully loose.

In Constraint Case 1 or "loose screw" condition, a screw can only apply compressive loads on the rotor. Modeling a screw that only pushes on an edge requires the use of non-linear gap elements (see §4.3). The screw was modeled as a rigid element[4] that was attached to the rotor by gap elements. The rigids were

[4]Rigid elements are 1-D elements with no elasticity or properties. Although, rigid elements should be used in situations where the material being represented by the rigid elements is be much harder than the surrounding material, representing the bolts with elements assigned the properties of steel versus representing them with rigid elements did not make significant changes in the solution.

constrained in all 6 degrees of freedom (DOF) at its center node. Rotational DOF are denoted with subscript "r".

In Constraint Case 2 or "tight screw" condition, the screw applies tensile loads on the rotor by the friction forces between the screw's bearing surface and the rotor's surface. The screw head was not modeled. Instead a simplified model where the screw can pull on the rotor at its thread contact interface was used. The nodes that line the bolt holes are connected to a rigid element. The central node of the rigid element is constrained in all 6 DOF.

Constraint Case 3 is difficult to simulate without multiple models because there is an infinite range between fully tight and fully loose conditions. Therefore, a pseudo model for case three was used. The "rotating tight screw" condition is the same as the tight screw condition but with the z_r DOF (rotation about the z axis) unconstrained at the the center node of each rigid element. Figure 5.4 shows the modeled constraint conditions. Stress distribution at the bolt holes from each Constraint Cases can be seen in Appendix B.

5.1.4 Modifications for Buckling Analysis

Linear buckling analysis was conducted using Optistruct. Buckling analysis requires that the shell elements be displaced out of plane, thus shear locking becomes a concern. For this reason, the rotors were remeshed primarily using quad elements interspersed with trias elements. Hypermesh was unable to create a mesh using purely quad elements. Constraints in the z direction at the pad-rotor contact patch also needed to be added to simulate the physical constraint that the brake pads place on the rotor under braking (see Figure 5.5). The result of an artificially stiff mesh caused by shear locking can be seen in Table 7.2.

5.1.5 Materials

Most mountain bike rotors today are made of a martensitic stainless steel for its strength, hardness, thermal resistance, and rust resistance [24]. SUS 403, 410, 420 are common types of stainless steel used for disc brake rotors. Although

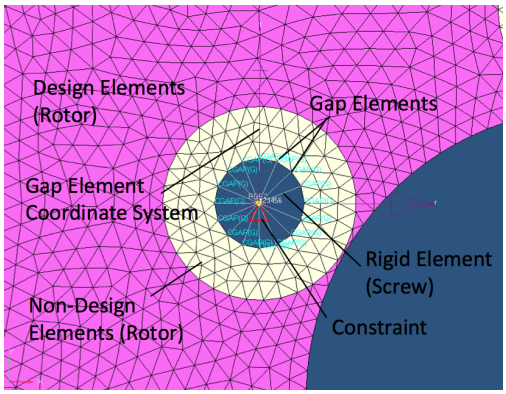

(a) Constraint Case 1: loose screw.

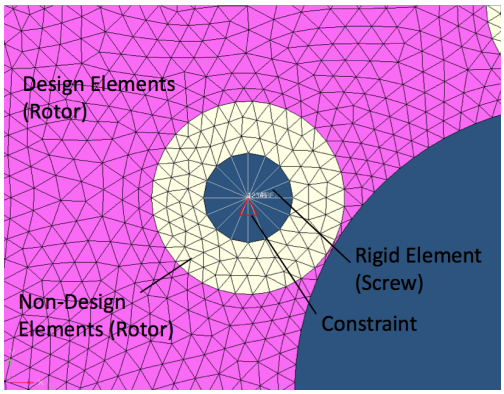

(b) Constraint Case 2: tight screw.

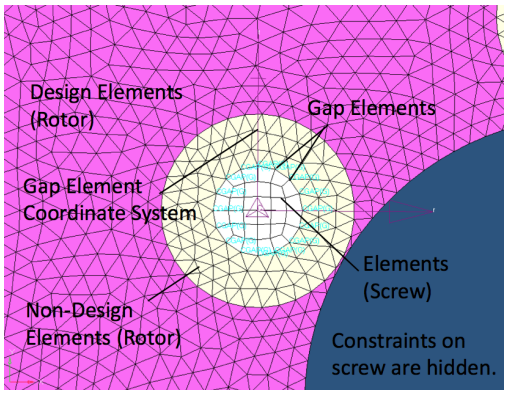

(c) Non-rigid screw.

Figure 5.4: Constraint cases and their modeled representation. Constraints for the non-rigid screw (c) are not shown, but all DOFs of the screw's center node are constrained. All other nodes on the non-rigid screw are constrained in only the z and z_r directions.

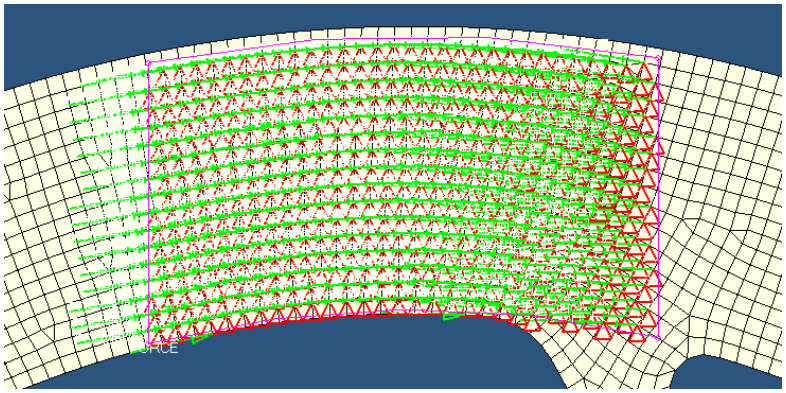

Figure 5.5: Quad elements and constraints at the pad-rotor interface in the z direction (in and out of the page). Changes made for buckling analysis.

rotors with aluminum mounts and stainless steel braking surfaces are becoming available, steel rotors are still prominent because of their ease of manufacture, and thus, reduced cost. There are numerous possibilities for multiple material designs that have yet to be tried, but the primary focus of this paper is an investigation of single alloy rotor design.

The grade of stainless steel is not readily available for each rotor. In this analysis it is assumed that all rotors are of the same grade of stainless steel, that they are under the same loading conditions, and that design advantages are purely from geometry. Therefore the exact material properties of the steel become unimportant when comparing the selected rotors. All rotor models were assigned default properties of a generic steel included in the Hypermesh package. The properties were as follows: Young's Modulus of 200 GPa, Poisson's Ratio of .3, and a density of 7.85 g/cm^3. These properties also fall within the ranges of martensitic stainless steel including SUS 403. The tensile strength and yield strength of SUS 403 was also used as a guideline for stresses that indicate where failure might occur; they are 485 MPa and 275 MPa, respectively[25].

5.2 Optimization

An optimization problem can be expressed mathematically with a cost function, which should include all considered design variables and their desired responses as introduced in §4.2. Optimization was conducted under different boundary conditions cases seen in §§5.1.3.

5.2.1 Design Space

The design space is the area which is to be optimized. Hypermesh makes it very easy to designate which elements are to be included in the optimization process and which elements will be unaffected. This is particularly important for structural optimization of the disc brake rotor, where material needs to be present around the rotor's mounting points and at its braking surface regardless of loading cases or rotor design. Figure 5.6 shows the design space, labeled as "Area 2", and the non-design area, labeled as "Area 1" and "Area 3." Area 1 is the braking surface of the disc and Area 3 consists of 6 regions surrounding mounting holes.

5.2.2 Design Response

The optimization goal is to reduce the weight of a disc brake rotor by removing material within the design space in a way that still allows for the discs to be manufactured by stamping. In other words, thickness must be uniform. Reducing weight by thinning the rotor is also not acceptable, because the rotor becomes more susceptible to warping when high temperatures are reached under braking. The temperatures seen by a bicycle rotor are not substantially lower than that seen by a motorcycle rotor [1]. The rotor is a body of uniform density, thus, either the mass or volume can be used as the response to minimize[5]. The "vol-

[5]Mass and massfrac responses are better for models where mass rather than volume is more important especially for models with non-uniform densities, or the volume is very small relative to the mass (high density). Volume and volfrac responses are better for models where volume is more significant than mass, and less dense models. For models with uniform density where mass or volume is not particularly more significant than the other, either response should give similar results [2].

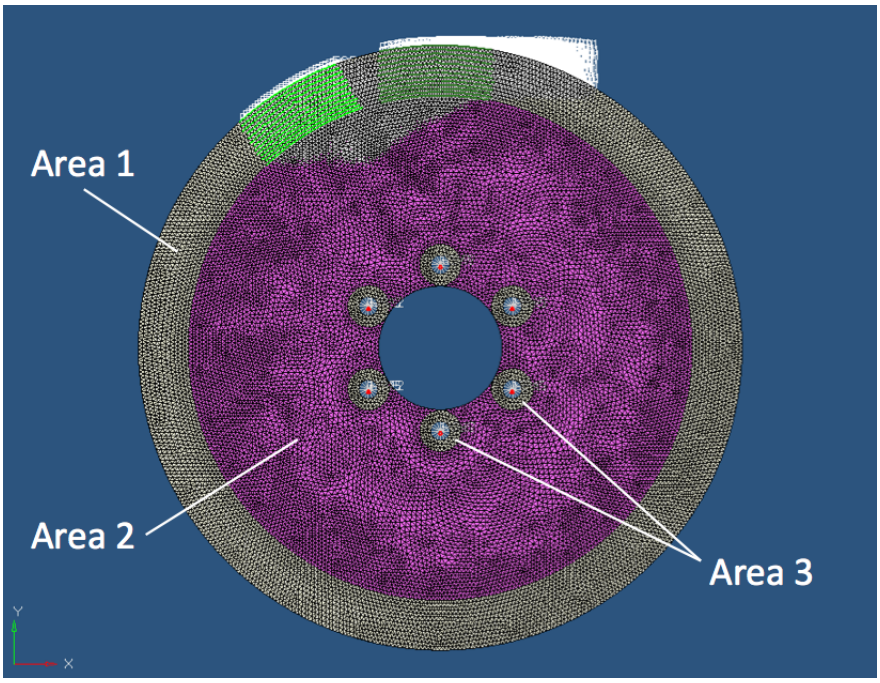

Figure 5.6: A meshed rotor with no material removed from the design area. The design area is labeled “Area 2”. The non-design area consisting of the braking surface and mounting holes are labeled “Area 1” and “Area 3.”

umefrac"response was used for optimization in Hypermesh. Volumefrac optimizes only the fraction of the volume designated for optimization; this is opposed to the "volume"response where optimization is done to the entire volume. The volume designated for optimization or design space is shown in Figure 5.6.

5.2.3 Optimization Constraints

Optimization constraints are conditions that must be satisfied when searching for the optimization solution (see §4.2). Stress and geometric symmetry were the only optimization constraints used.

Stress Constraint

There are few regulations on the performance of a bicycle disc brake rotor, only that it much be able to decelerate a rider as specified[9]. The tensile strength of a commonly used stainless steel for rotors, SUS 403 is 485 MPa [24][25]. Therefore, 485 MPa was initially used as the stress constraint for a limit state design case. However, the optimization solutions contain stresses that exceeded stress level ceilings defined by the stress constraint for all BC condition cases. Optistruct is a gradient based solver (see §4.3). These solvers are prone to getting stuck in local minima of the cost function's search space. It is possible that solutions found are not the global minima of their relative search spaces of their cost functions. Also, stress constrained optimization problems are difficult to solve; using stress as an optimization constraint has its limitations[6]. For this reason, several subsequent constraint cases, including the permissible stress design case, were implemented in the optimization. Stress constraints of 450, 400, 350, 300, 275, and 250 MPa were applied. The optimization problem with stress constraint of 275 MPa is the

[6]There are several limitations when using the stress constraint for topology optimization: (1)Only a single von Mises stress constraint can be placed on a model. Singular topology is apparent when a structure contains several materials each with its own stress constraint. This can lead to solutions that cannot be found by a gradient based solver such as Optistruct. (2)Stress constraints on a partial domain is not allowed and is applied to the entire model including non-design areas. (3)Optistruct is capable of filtering out artificial stress concentrations from point loads and BCs, but are only partially filtered for stress concentrations from boundary geometry. These are improved more effectively with local shape optimization.[2]

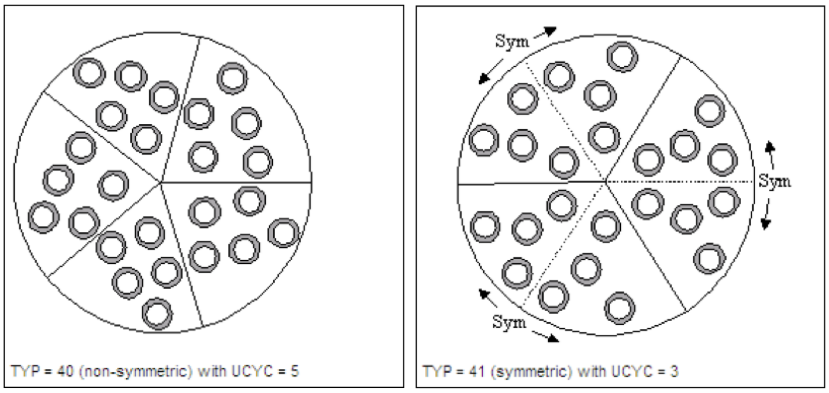

(a) cyclic symmetry (b) cyclic, 1 plane symmetry

Figure 5.7: Symmetry constraints used during optimization. Source:[2]

permissible stress design case. The optimization solutions under various stress constraints can be found in Figures 6.2 through 6.7.

Symmetry Constraint

The symmetry constraint forces the optimization solution to be symmetric in the specified manner, regardless of the initial mesh, boundary conditions or loads [2]. Cyclic symmetry and cyclic, one plane symmetry were used for this work. Cyclic symmetry divides the design area into equal parts and finds a solution that has the same geometry in each section. Cyclic, one plane symmetry also divides the design area into equal parts with the same geometry within each section, but has an additional requirement that forces the solution to be symmetric about a plane that bisects each cyclic segment. The number of parts is specified by the user. An example of each are shown in Figure 5.7.

The cyclic symmetry of six parts was used for optimizing the disc brake rotor, because of the cyclic symmetry that the six hole mounting pattern creates. This allows for the set up of only one load case to create an optimization solution for six angularly repeated loads. As discussed in §§5.1.3 the rotor was optimized for multiple orientations, represented by two load cases each with a six part cyclic symmetry constraint.

Chapter 6

Optimization Solutions

Optimization solutions resulting from various boundary conditions and optimization constraints can be seen in Figures 6.2 through 6.7. The optimization solution that lead to the final design is shown in Figure 6.6(e).

These solutions should not be used directly as the final optimized design. The solutions show "element densities" which can be interpreted as a normalized thickness. Elements of what density should be removed, as well as any other smaller change, is ultimately dependent on the designer. Even when select elements are removed the profile of the rotor follows the boundary of the model elements. Variation in the thicknesses of the rotor is not acceptable because of how actual rotors are manufactured. Also, the solution does not include design considerations for smaller geometric boundary details that affect stress such as radii of curvature. If additional and more localized optimization is desired, size and shape optimizations can be performed with Optistruct[2]. Even then, the solutions should be combined with the design knowledge and experience of an engineer to create a manufacturable part. Once a part is designed, reanalyzing the designed part is needed to verify that it will perform as necessary. Optimization solutions should be used as a guide for designing actual parts.

Several designs that were very close to the optimization results were created that did not perform as well as desired, relative to rotors A and B. Some of these designs and their stress distributions can be found in Appendix D. Although some

of these rotor designs can be improved by shape and size optimizations, it would be time consuming to make a design based on each of the optimization solutions, especially because the final rotor design should be able to perform well in all three constraint conditions. Fortunately, several significant observations can be made from the solutions obtained.

There are three reoccurring general geometries that appear throughout the solutions. They resemble a rotary tiller blade or a "λ" symbol cyclically patterned about the disk's center, an "X" cyclically patterned about the disk's center, and a six sized star. These patterns are here on referred to as the "tiller" pattern, "X" pattern, and "star" pattern, respectively. Respective examples of each are shown in Figures 6.2(a), 6.4(e), and 6.5(a). The X and star patterns are truss-like patterns arranged radially about the center of the rotor, and are collectively referred to as truss type patterns. Existing single-alloy rotors almost exclusively resemble the tiller type pattern. This is very interesting given the number of truss type optimization solutions found. Though these designs may look like very different solutions, they are probably near each other in the optimization search space. The tiller and star patterns are variants of the X pattern: the tiller pattern is the X pattern with an arm missing from each of the X structures and the star pattern is the X pattern with each X structure's upper arms spread until they touch the adjacent X structures. This becomes more apparent when looking at the design iterations that result in each type of solution. Some iterations in the optimization process are shown in Appendix E for a solution that results in each of the three above mentioned patterns. Although not all iterations are shown, it is clear that the solutions are very similar until the last iterations of the design process. This suggests that an optimal design for varying constraint conditions may be from a combination of these various solutions. There are also some solutions that very clearly will not work for other constraint conditions, such as the solution in Figure 6.3(f).

Mirrored tiller patterns such as those in Figures 6.3(a) and 6.3(b) or Figures 6.4(a) and 6.4(c) prompted analysis done in §7.2. They suggest that direction of operation may not be significant even in existing rotors that have the direction of

use inscribed on the surface of the rotor.

Examining the optimization solutions also makes apparent that the solutions are not necessarily the best solution that exist, but the best solution found by the optimization algorithm within the search space of the cost function. It is possible for the algorithm to get stuck in a local minima of the search space, since the algorithms used by Optistruct are gradient based methods (see §§5.2.3). It is expected that as the stress constraints become lower (lower allowed stress), more material will be added to the rotor. Although the majority of the solutions show the expected trend, Figures 6.5(b) and 6.6(f) show the contrary. This is an additional reason than the optimization solutions cannot simply be used as the final design.

There are also interesting observations to be made on solutions with lower stress constraints. For "loose" constraint conditions in both cyclic and cyclic, 1-plane symmetry cases, and stress constraints of 250 MPa the solution given was an unaltered generic disk. Under the same physical constraints with a stress constraint of 275 MPa, any distinct geometry manufacturable by stamping is not defined. This means that under these loading conditions designing a rotor that will have stresses under 275 MPa that is lighter than existing rotors is probably not likely. At stress constraints of 300 MPa, manufacturable solutions exist. They are of special interest because they are the designs closest to permissible stress design.

Processing was done on a MacBook Pro running Windows XP through Parallels^{TM} with a 2.16GHz Intel CoreDuo chip and 1 GB of RAM. With about 275 MB of alloted memory, processing times for optimization were around 15 min for models constrained by 0 DOF rigids, 25 min for models constrained using 1 DOF rigids, and 1.5 hours for models constrained by gap elements. Solutions from models with gap elements take a significantly longer time to obtain because of the additional iterations necessary for gap element analysis.

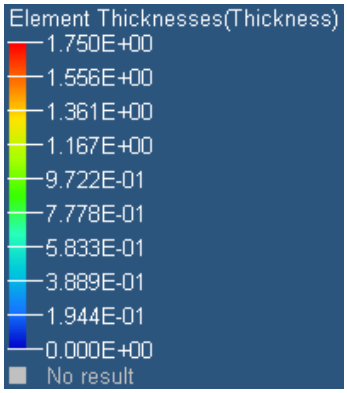

Figure 6.1: Legend for optimization solutions (Figures 6.2 through 6.7): thickness in mm.

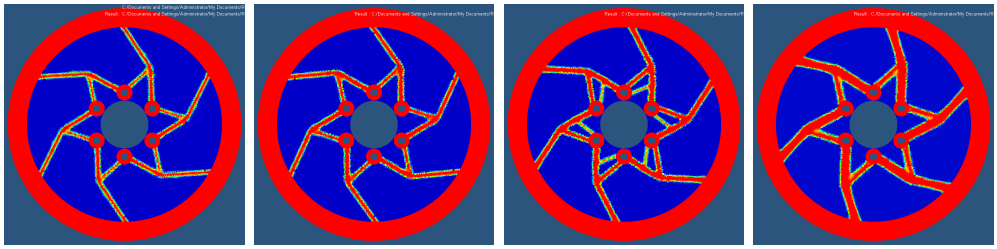

(a) 485 MPa (b) 450 MPa (c) 400 MPa (d) 350 MPa

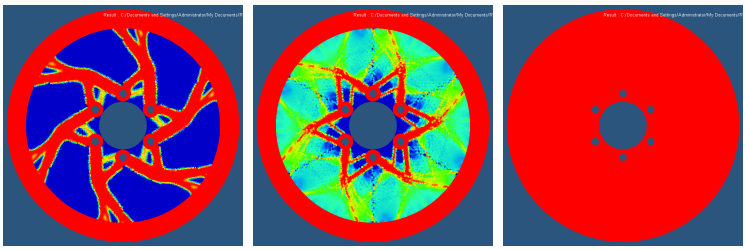

(e) 300 MPa (f) 275 MPa (g) 250 MPa

Figure 6.2: Optimization solutions resultant from 6 part cyclical symmetry and various stress constraints. “Loose screw” physical constraints were used.

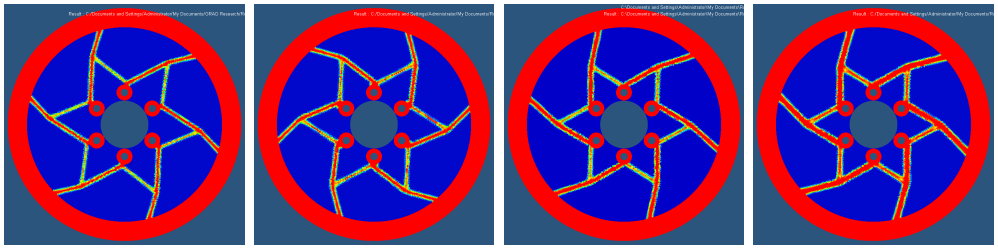

(a) 485 MPa (b) 450 MPa (c) 400 MPa (d) 350 MPa

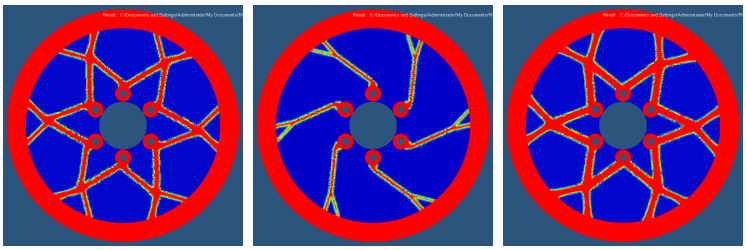

(e) 300 MPa (f) 275 MPa (g) 250 MPa

Figure 6.3: Optimization solutions resultant from 6 part cyclical symmetry and various stress constraints. "Tight screw" physical constraints were used.

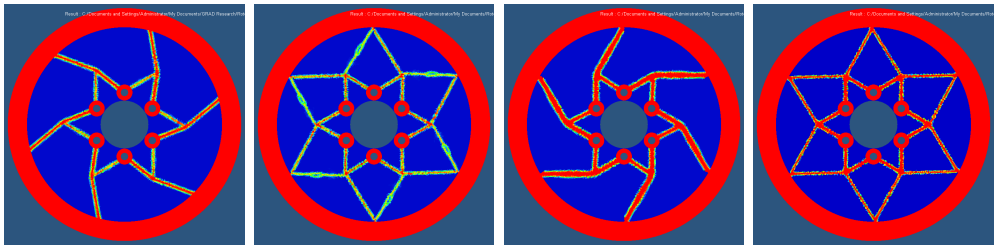

(a) 485 MPa (b) 450 MPa (c) 400 MPa (d) 350 MPa

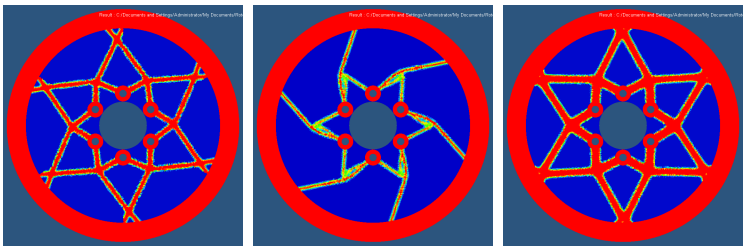

(e) 300 MPa (f) 275 MPa (g) 250 MPa

Figure 6.4: Optimization solutions resultant from 6 part cyclical symmetry and various stress constraints. "Rotating tight screw" physical constraints were used.

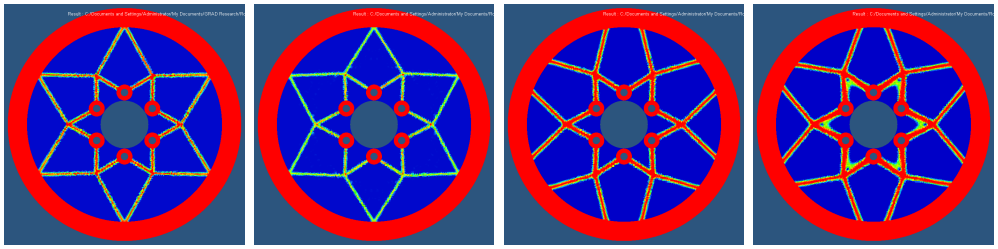

(a) 485 MPa (b) 450 MPa (c) 400 MPa (d) 350 MPa

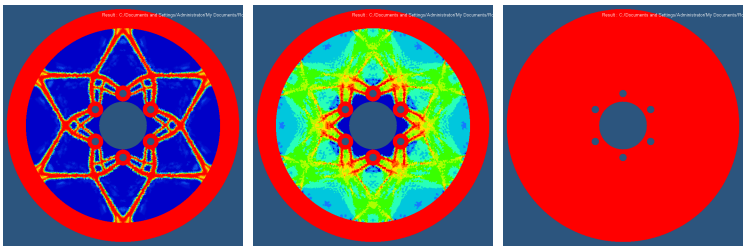

(e) 300 MPa (f) 275 MPa (g) 250 MPa

Figure 6.5: Optimization solutions resultant from 6 part cyclical, 1-plane symmetry and various stress constraints. "Loose screw" physical constraints were used.

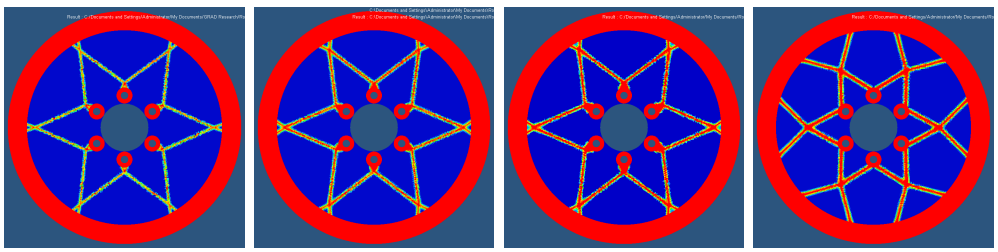

(a) 485 MPa (b) 450 MPa (c) 400 MPa (d) 350 MPa

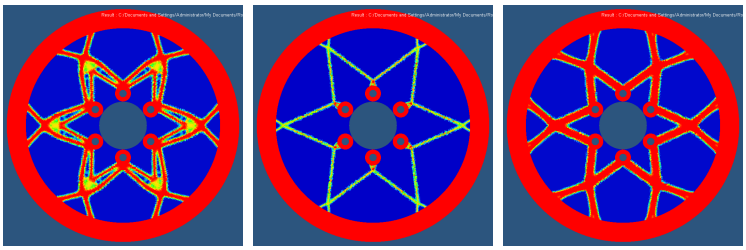

(e) 300 MPa (f) 275 MPa (g) 250 MPa

Figure 6.6: Optimization solutions resultant from 6 part cyclical, 1-plane symmetry and various stress constraints. "Tight screw" physical constraints were used.

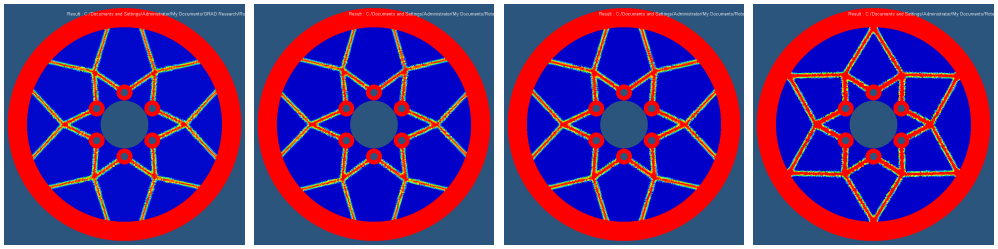

(a) 485 MPa (b) 450 MPa (c) 400 MPa (d) 350 MPa

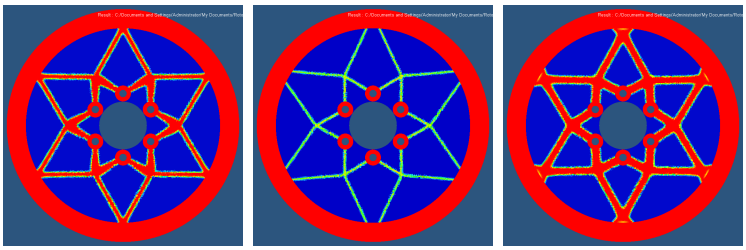

(e) 300 MPa (f) 275 MPa (g) 250 MPa

Figure 6.7: Optimization solutions resultant from 6 part cyclical, 1-plane symmetry and various stress constraints. "Rotating tight screw" physical constraints were used.

Chapter 7

Post-Processing and Analysis

7.1 Analysis of Existing Designs

It is necessary to compare the new design to existing designs to determine quantitative improvements. Comparison with existing rotors also ensures that the new design is safe for normal use even if the magnitudes of forces or strengths of materials happen to be different than expected during optimization; all rotors are evaluated under the same conditions and properties. The only difference is the geometry of the rotor inside the designated design area (see §§5.2.1). Rotor designs from Hayes^{TM} and Shimano^{TM} were chosen as base comparisons for the final rotor design. Both companies are very popular and successful in the mountain biking industry. Their rotors have a relatively long history of use and are widely used in the mountain bike communities at all levels, including the most extreme professional athletes[26][27]. Figures A.2 and A.3 show the respective Hayes and Shimano rotors and the Solidworks models imported into Hyperworks for preprocessing. From here on the Hayes rotor is referred to as "Rotor A" and the Shimano rotor is referred to as "Rotor B." The surface area of the rotor's face[1] for the Rotor A and Rotor B are 11,199.15 mm^2 and 10,956.31 mm^2, respectively. With rotor

[1]This is the surface area of the model. Holes in the braking surface that exist in the actual rotors are not included in models or analysis.

thickness of 1.75 mm and material density of 7.85 g/cm^3, this correlates to a mass[2] of 153.85 g and 150.51 g for Rotor A and Rotor B, respectively. Considering moments of inertia, equivalent masses can be calculated using Equation 3.25 as well. The moment of inertia[3] about the rotors' rotational axis for Rotor A and B are 617,255 g-mm^3 and 566,232 g-mm^3, respectively. Equivalent masses for Rotor A and B are 177.96 g and 172.63 g, respectively.

Both rotors are 160 mm diameter discs, have the standard 6 bolt mounting pattern, and brake pad contact surfaces, but have little more in common. The holes in the brake pad contact surface (outer ring of the rotor) are primarily for debris removal, prevention fluid film layers, and some heat dissapation; their size and shape vary from rotor to rotor as well. The affect of the friction surface's geometric variations were not analyzed.

Geometry from Solidworks was imported into Hyperworks and preprocessed the same way the optimization problems were set up without the optimization parameters. By using the same BCs and mesh size it is possible to directly compare the stress distribution within each rotor. Figures 7.2 and 7.3 show the stress distribution within Rotor A and Rotor B, respectively. Localized stresses around the mounting holes in the loose screw case for Rotor B are above the tensile stress of the steel used. This analysis was done on a linear solver so plastic deformation is not considered. Thus, this may not be an accurate representation of actual stresses in the rotor, because it is near the tensile strength of the material, where plastic deformation is likely to occur. However, it is also possible that the applied loads to the rotor are actually higher than typically seen, or that the rotors were never designed for the loose screw case; minimum torque levels for the screws when mounting to the hub are provided with the rotor in the mounting instructions. The rotors' strength was determined by the maximum stress excluding localized stresses around the mounting holes, here on referred to as the "stress limit". Maximum

[2]This is the mass of the model. Holes in the braking surface that exist in the actual rotors are not included in models or analysis. Also, the type of steel used in the actual rotors is unknown so actual and used densities may differ slightly.

[3]Moments of inertia are from Solidworks models without holes in the braking surface that exist in the actual rotors. Moments of inertia of actual rotors are lower than stated values due to these holes.

stresses including and excluding localized stress around mounting holes for each mounting and load condition are shown in Table 7.1. The stress limits for the Rotor A and Rotor B were 396.3 MPa and 349.6 MPa, respectively. A stress limit in this range is desired for the new rotor design under the same BCs.

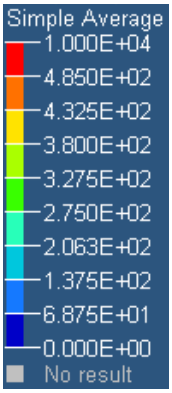

Figure 7.1: Legend for Figures 7.2 and 7.3: Stress in MPa

7.2 Reverse Loading and Buckling Analysis

Existing rotors are meant to be loaded in one direction only. The direction of rotation is inscribed on each rotor. However, optimization results in Figures 6.3 and 6.4 show tiller patterns that are opposite the expected tiller pattern direction. To investigate how important it is to load the rotor in the correct direction, stress analysis on Rotor B under reverse loading was conducted. Figures 7.5 and 7.6 show the stress distribution in the rotor under normal and reverse loadings. There is little change in the stress distributions except that the tensile stresses become compressive stresses and compressive stresses become tensile stresses of the same magnitude even when the rotor is in the loose screw condition (except areas around the mounting holes). Although this analysis and the optimization solutions suggests that the direction of rotation of the rotor is not important, additional buckling analysis is necessary to understand why one direction is preferred over the other.

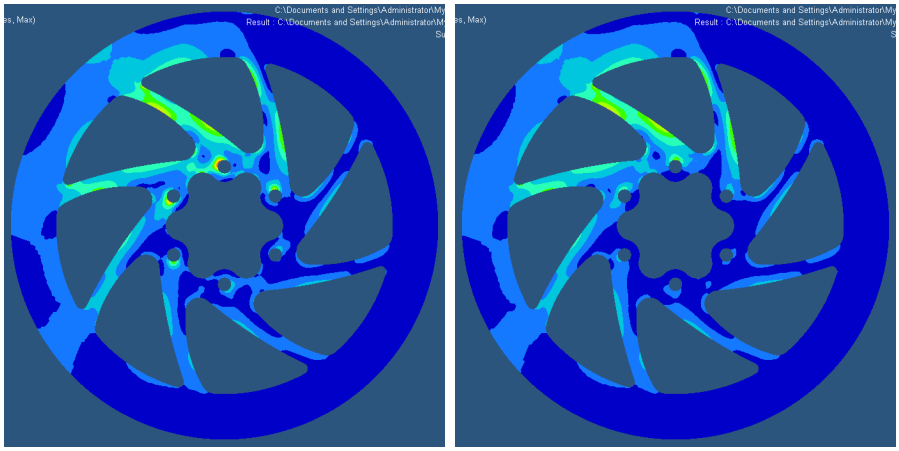

(a) Load 1, Loose screw

(b) Load 1, Tight screw

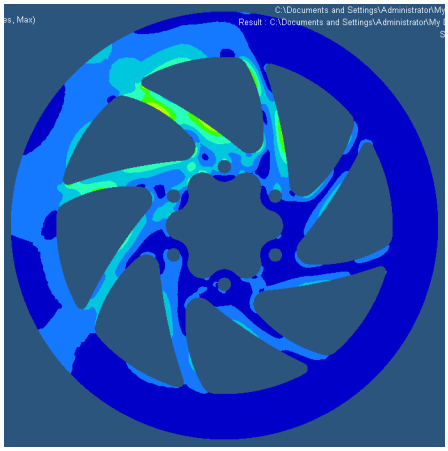

(c) Load 1, Rotate screw

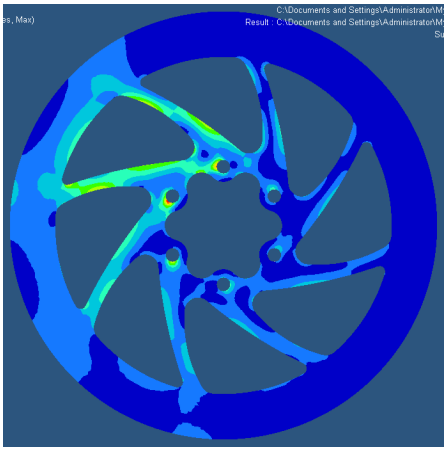

(d) Load 2, Loose screw

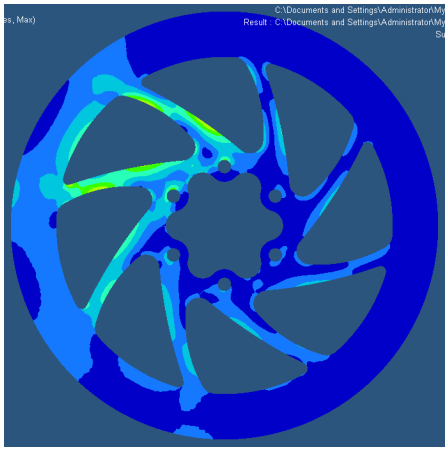

(e) Load 2, Tight screw

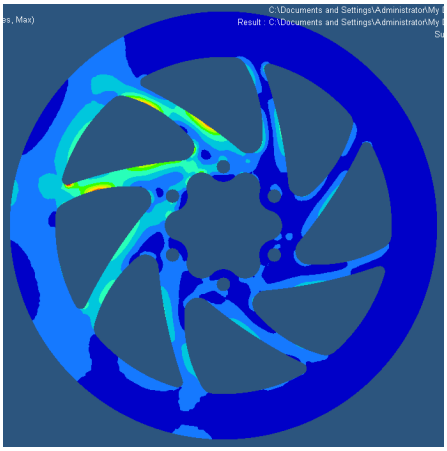

(f) Load 2, Rotate screw

Figure 7.2: Von Mises Stress distribution in Rotor A under various load and mounting conditions.

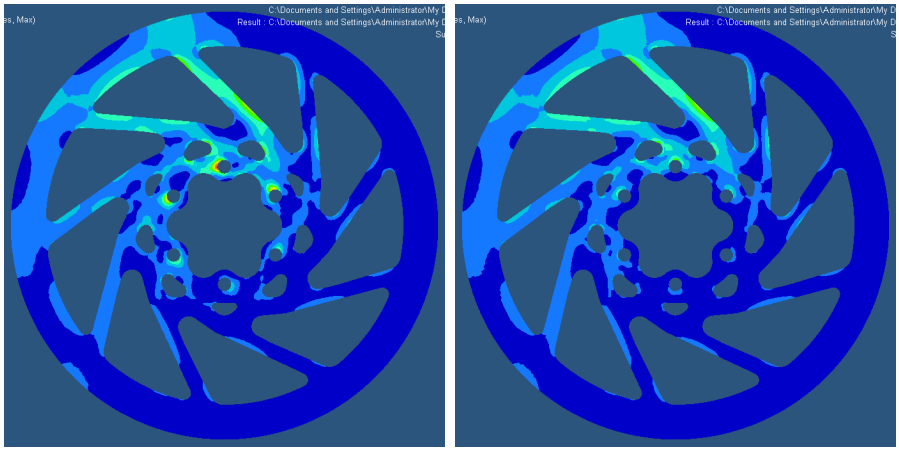

(a) Load 1, Loose screw

(b) Load 1, Tight screw

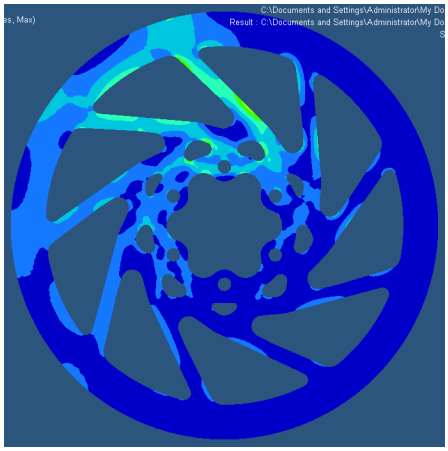

(c) Load 1, Rotate screw

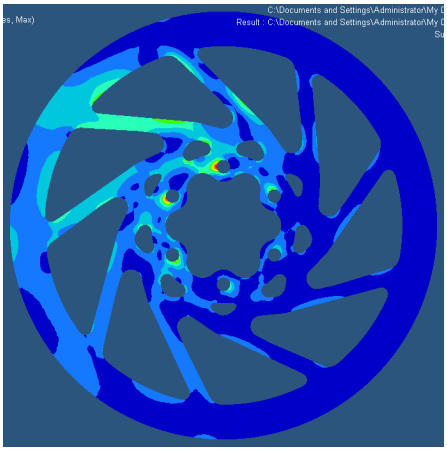

(d) Load 1, Loose screw

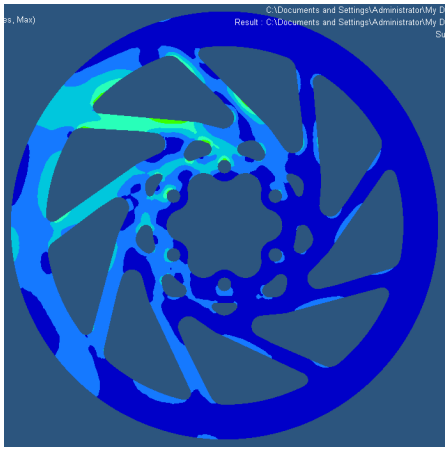

(e) Load 1, Tight screw

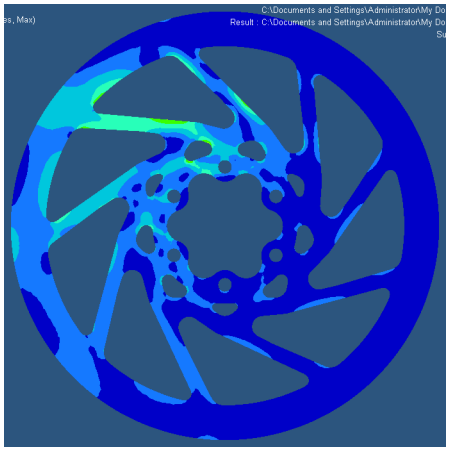

(f) Load 1, Rotate screw

Figure 7.3: Von Mises Stress distribution in Rotor B under various load and mounting conditions.

Table 7.1: Maximum Stresses in Rotors

Bound.	Cond.	Rotor A		Rotor B		New Design	
		stress about holes		stress about holes		stress about holes	
		included	excluded	included	excluded	included	excluded
Load 1	Loose	480.5	396.3	541.8	349.6	390.3	369.8
	Rotate	394.2	394.2	349.3	349.3	390.8	390.8
	Tight	392.9	392.9	347.2	347.2	390.8	390.8
Load 2	Loose	489.5	390.7	550.4	326.9	350.0	350.0
	Rotate	389.2	389.2	348.1	348.1	349.3	349.3
	Tight	381.0	381.0	334.3	334.3	375.5	375.5

Stresses in MPa.

Generally for ductile materials, the ultimate compressive strength of a material is higher than its ultimate tensile strength because the cross-sectional area increases, rather than decreases, as the limit is reached [28]. This would suggest that the original direction of rotation is preferable. However, loading in the original direction may make the rotor prone to buckling because of the compressive loads on the long thin members that run from the braking surface to the center of the rotor. The best direction of rotation is dependent on whether structural failure due to tensile strength or buckling will occur first.

Table 7.2 shows the buckling factors for the first 10 buckling modes. Buckling shapes of each mode are shown in Appendix F. Negative buckling factors mean that buckling is likely with loading in the opposite direction. Buckling factors for all three rotors at all modes are greater than one, which suggests that buckling is unlikely with the 4000N load applied. Therefore, structural failure is the limit that determines rotor direction, and the original loading direction that puts the thin members in compression is preferred. Buckling analysis on Rotor A using only trais elements was done for comparison. The higher buckling factors are the result of an artificially stiff mesh caused by shear locking.

7.3 Final Rotor Design

The optimization solutions were exported to Solidworks as an IGES file to be used as a guide for the new rotor's geometry. The geometries were put back into Hypermesh to be analyzed. Variations of initial designs were made to satisfy stress requirements, determined by Rotor A and Rotor B. The new rotor design is illustrated in Figure 7.7. The rotor design is based on the solution in Figure 6.6(e). This solution is under the tight screw constraint. Because rotation about the mounting holes is not free, the solution tends to give geometries that will have large moments on them when the mounting points become unconstrained in the z_r direction. The vertex, where the two lower arms of the "X" structure meet the adjacent X structure above the mounting hole, was shifted to coincide with the center of the mounting hole, eliminating stresses caused by the moments from that

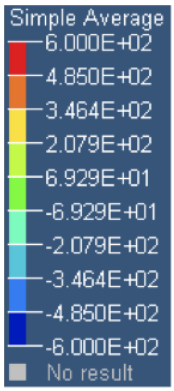

Figure 7.4: Legend for Figures 7.5 and 7.6: Stress in MPa (+tension, -compression)

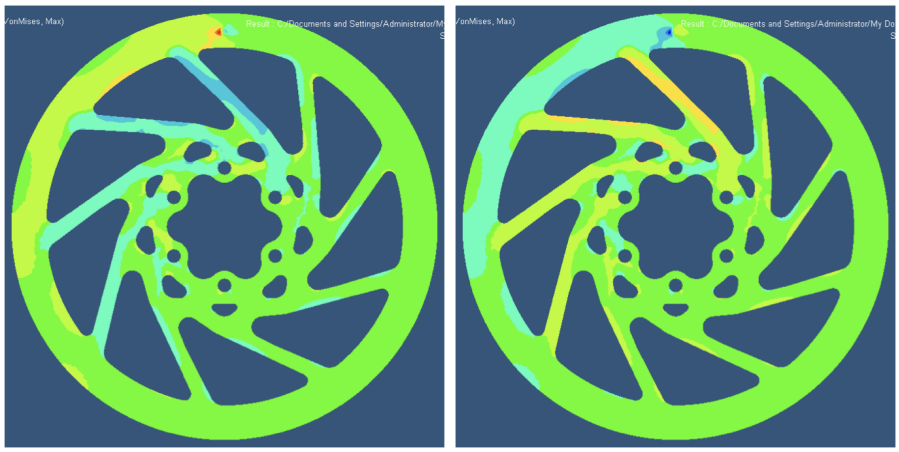

(a) Recommend loading direction (braking force to the right at top of rotor).

(b) Reverse loading direction (braking force to the left at top of rotor).

Figure 7.5: Signed Von Mises Stress distribution in Rotor B when loads are reversed (backwards mounting) in tight screw conditions

Table 7.2: Buckling Factors of First 10 Modes

Mode	Rotor A				Rotor B		New Design	
	tria		quad		quad		quad	
	Load 1	Load2	Load 1	Load2	Load 1	Load2	Load 1	Load2
1	1.63	1.64	1.61	1.63	-1.81	-1.88	3.24	3.59
2	-1.84	-1.75	-1.82	-1.74	2.12	2.14	-3.26	-3.63
3	-2.02	-2.07	-1.99	-2.06	-2.25	-2.25	-3.85	-3.95
4	-3.41	-3.59	-3.36	-3.57	-3.83	-3.79	3.87	3.95
5	3.91	3.85	3.85	3.80	-4.26	-4.39	4.20	4.25
6	-4.04	-3.90	-3.98	-3.88	4.81	4.89	-4.23	-4.27
7	4.68	5.13	4.62	5.10	5.67	5.11	-6.32	7.28
8	-5.70	5.75	-5.61	5.70	-6.23	-6.14	6.33	-7.39
9	5.71	-5.76	5.63	-5.73	6.47	6.61	-7.16	-7.79
10	-6.26	-6.46	-6.16	-6.41	-7.00	6.98	7.23	7.83

Negative buckling factors are buckling modes that occur under reverse loading.

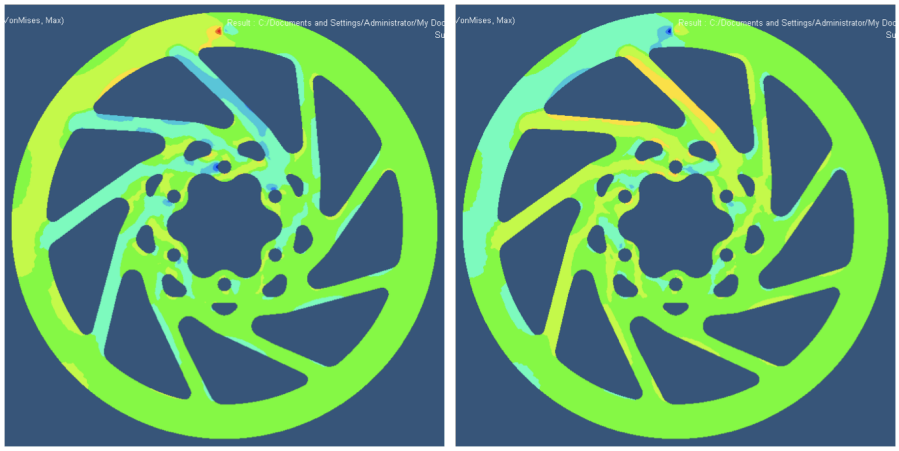

(a) Recommend loading direction (b) Reverse loading direction

Figure 7.6: Signed Von Mises Stress distribution in Rotor B when loads are reversed (backwards mounting) in loose screw conditions

additional distance. Stresses for the design in Figure 7.7(a) can be found in Figure D.1(a) in Appendix D. Note that the high stresses in the inner lower arms of the X structure present in the first iteration design are not present in the final disc design. Also, note that the final design also resembles the optimization solution in Figure 6.5(e). This supports observations made in §6.

A new lighter rotor design with strength comparable to rotors A and B was obtained, but possibilities for even lighter rotors with the same strength exist. The new rotor is the final product of several iterations of analysis and geometric tweaking. This can be done more effectively with size and shape optimization.

The area of the new rotor's face is 9,594.24 mm^2. With a rotor thickness of 1.75 mm and material density of 7.85 g/cm^3, this corresponds to 131.80 g. This is a 14.3% improvement over Rotor A and a 12.4% improvement over Rotor B. The moment of inertia about the rotational axis of the new rotor is 538,234 g-mm^3. Thus its equivalent mass is 152.87 g. Using equivalent masses, improvements are 14.1% and 11.5% over Rotors A and B, respectively.

Analysis on the new rotor was done under both loading conditions and all mounting conditions. The stress distribution of the new rotor in all cases can

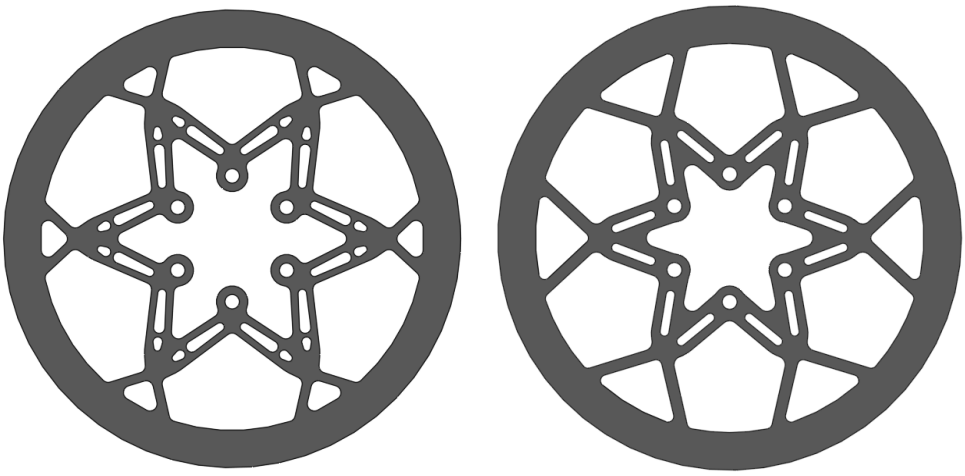

(a) First iteration design from solution (b) Final design (second iteration)

Figure 7.7: New disc brake rotor and its previous iteration designs. Designs based off of optimization solution shown in Figure 6.6(e).

be found in Figure 7.9. The stress limit[4] in the new design is 390.3 MPa. This is a 1.4% improvement over Rotor A and 10.5% worse than Rotor B. However, Rotor A is 11.5% weaker than Rotor B. Meeting only the stress levels of Rotor B is sufficient, because Rotor B has worked without failure under normal use in practice. If the maximum stresses are used the new disk is 20.1% stronger than Rotor A and 29% stronger than Rotor B. In the new rotor, maximum stresses seen are fairly uniform across all loading and mounting condition. Much larger stresses are seen in rotors A and B under the loose screw condition. Maximum stresses under each boundary condition can be seen in Table 7.1.

It may seem unusual that such an improvement can be made when very few, if any, single alloy bicycle brake rotors use this kind of truss-like design. However, when motorcycle brake rotors and newly available multi-alloy bicycle disk brakes are examined the result is less surprising (see Figure A.5 and Figure A.6). Both tiller type designs and truss type design are widespread and common. It is possible that because disc brakes on motorcycles have been around for a much longer time, reach higher loads, and receive more stringent regulations as a motorized vehi-

[4]See §7.1

cle component, their disc brake rotors have undergone more thorough designing. Advanced computational resources are become more readily available, leading to better designs in both motorcycle and bicycle rotors. In any case, parallels seen between bicycle rotor design and motor cycle rotor design, support the findings in this work.

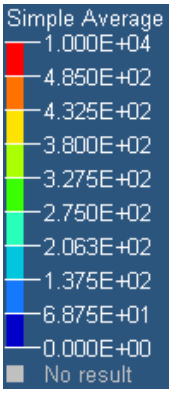

Figure 7.8: Legend for Figure 7.9: Stress in MPa

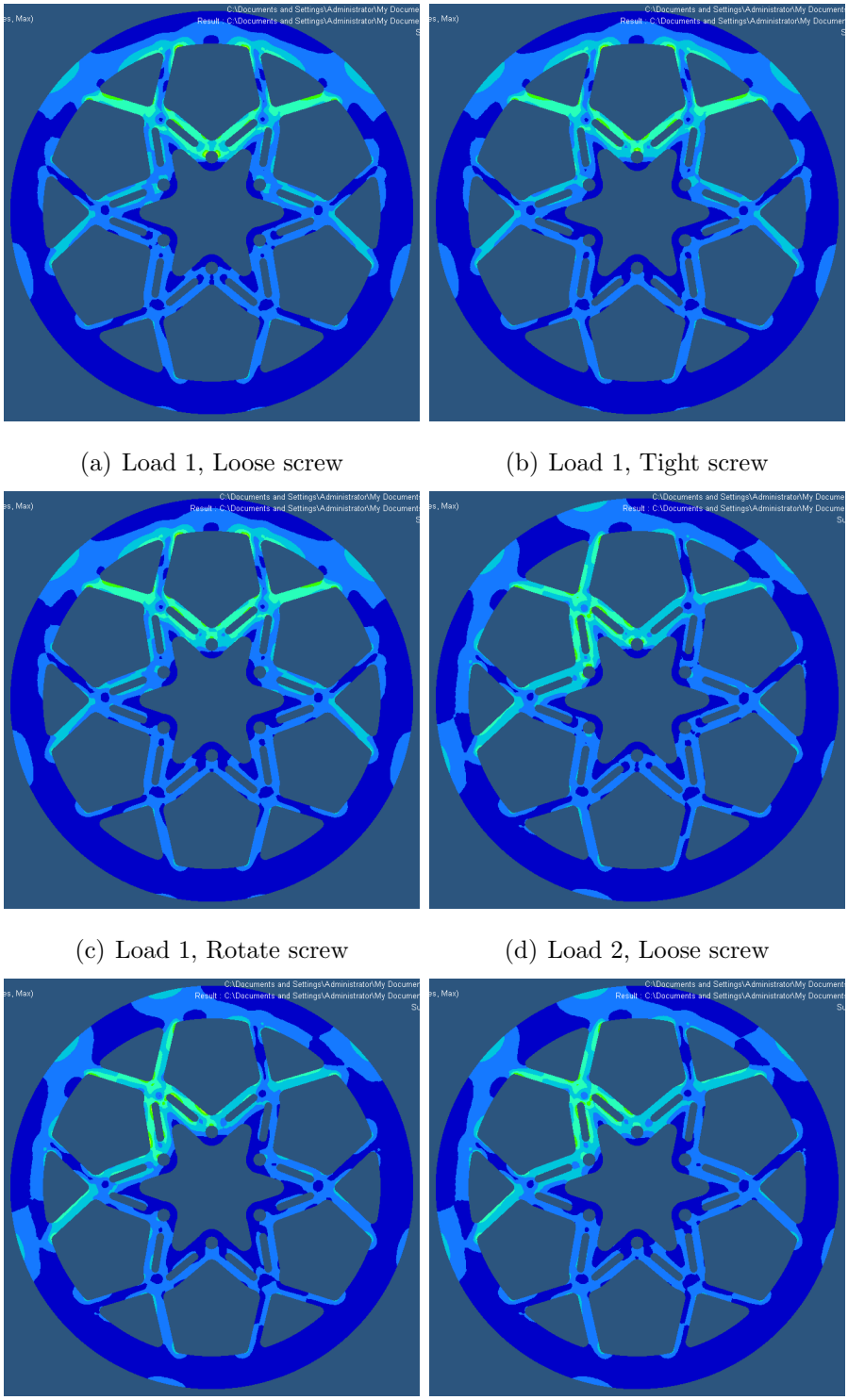

(a) Load 1, Loose screw

(b) Load 1, Tight screw

(c) Load 1, Rotate screw

(d) Load 2, Loose screw

(e) Load 2, Tight screw

(f) Load 2, Rotate screw

Figure 7.9: Von Mises Stress distribution in the new rotor under various load and mounting conditions.

Chapter 8

Conclusion

The structural design of rotors used for bicycle disc brake systems vary greatly from company to company as well as within individual companies. The lightest possible rotor without compromising strength is desired, however, which design features that help lead to a light strong rotor are not obvious. Topology optimization on a disc brake rotor was performed using linear finite element models solved by Optistruct. Analysis and optimization does not account for any cyclic loading, plastic deformations, or heat effects. Objectives were to design a lighter rotor with similar strength relative to existing rotors available commercially and to investigate the reasons behind the large variety in rotor designs. Although multiple alloy rotors are becoming more commonplace, focus was on single alloy rotors because of their reduced manufacturing costs. The reduced manufacturing costs and their length of availability in the marketplace still make single alloy rotors the large majority of rotors used. Popularity of single alloy rotors will probably continue unless multi alloy rotor costs are significantly reduced.

Some optimization solutions from the finite element models resembled the rotary "tiller" structure found almost exclusively in commercially available single-alloy rotors. However, a large number of solutions for truss type structures were found. The final rotor design is based on a truss type solution whose performance was found to be better than existing rotors. The new rotor's strength was similar to commercially available Rotor A and Rotor B, while being 14.3% lighter than

Rotor A and 12.4% lighter than Rotor B. The truss type design is unconventional in single alloy bicycle disc brake rotors, however, the design's validity is supported by existing brake rotors found in multi-alloy bicycle rotors and motorcycle rotors.

Appendix A

Bicycle and Rotor Figures

Figure A.1: Diagram of the majors parts of a full suspension bicycle. [4]

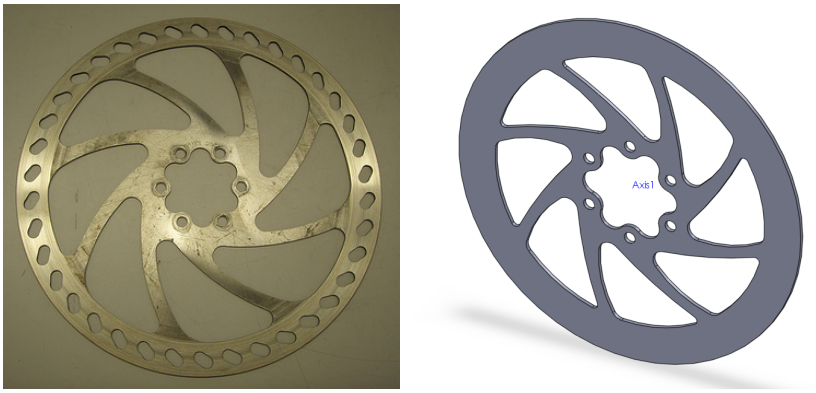

(a) Photo (b) Solidworks model

Figure A.2: A Hayes disc brake rotor (Rotor A).

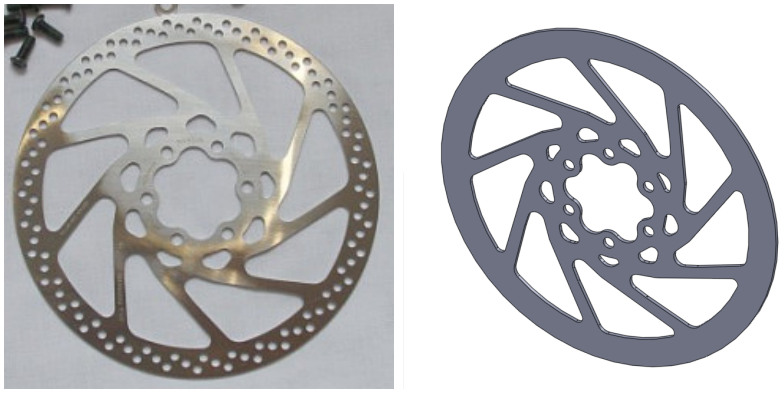

(a) Photo (b) Solidworks model

Figure A.3: A Shimano disc brake rotor (Rotor B).

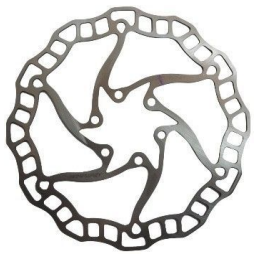

(a) Ashima rotor [29]

(b) Formula rotor [30]

(c) Formula rotor [30]

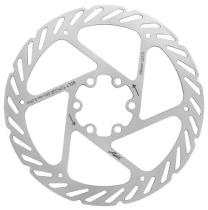

(d) Avid rotor [31]

(e) Avid rotor [31]

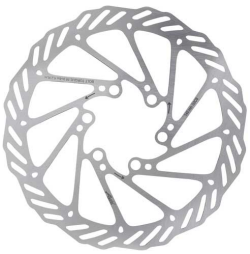

(f) Avid rotor [31]

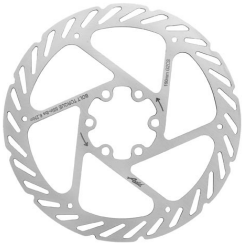

(g) Avid rotor [31]

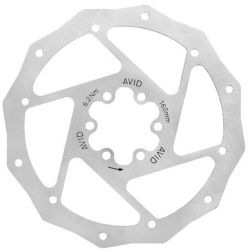

(h) Avid rotor [31]

(i) Magura rotor [32]

(j) Shimano rotor [33]

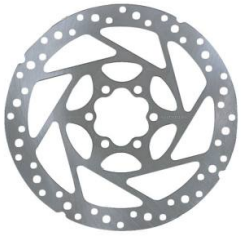

(k) Shimano rotor [33]

(l) Hayes rotor [34]

(m) Dirty Dog rotors [35]

Figure A.4: Examples of the widely varying designs within and throughout various companies that sell bicycle disc brake rotors. Source: Listed with respective figures.

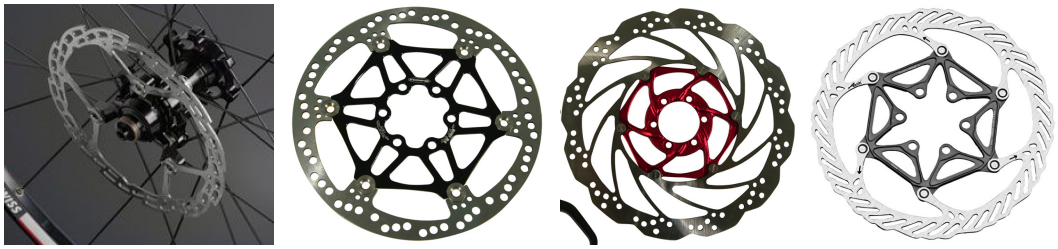

(a) Hope rotor [36] (b) Hope rotor [36] (c) Magura rotor [32] (d) Avid rotor [31]

Figure A.5: Examples of multi-alloy designs for bicycle disc brake rotors. Source: Listed with respective figures.

(a) EBC rotor [37] (b) Brembo rotor [37] (c) Brembo rotor [37] (d) Brembo MotoGP rotor [38]

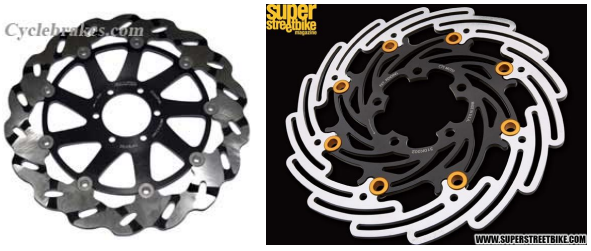

(e) Galfer rotor [37] (f) CTS rotor [39]

Figure A.6: Examples of various motorcycle rotor designs. Both truss and tiller type designs are common. Source: Listed with respective figures.

Appendix B

Screw Modelling Analysis

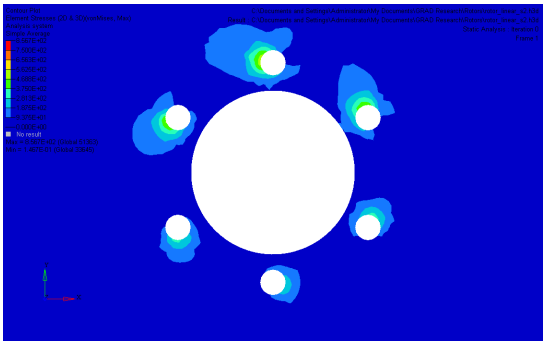

(a) loose screw condition

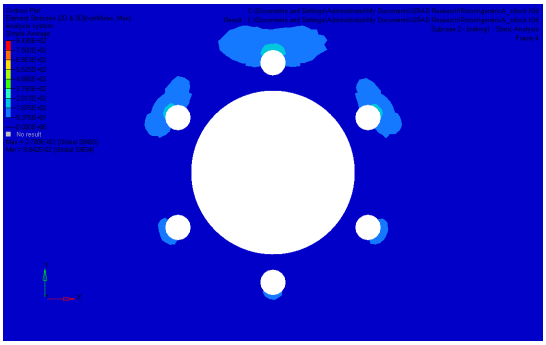

(b) tight screw condition

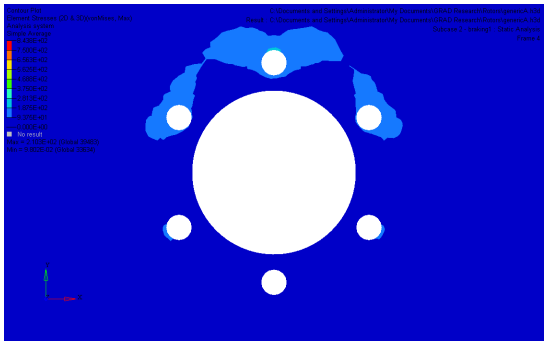

(c) rotating tight screw condition

Figure B.1: Stress concentrations in the rotor at the mounting holes.

Appendix C

Load Case Modeling Analyses

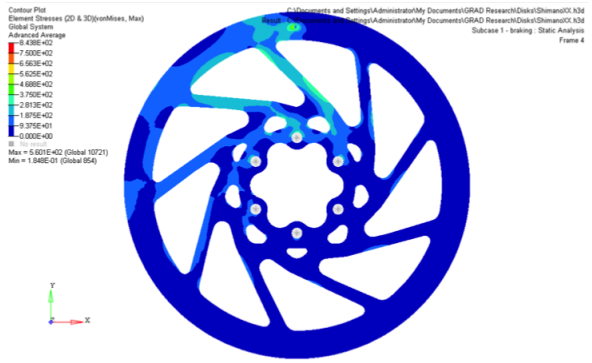

(a)

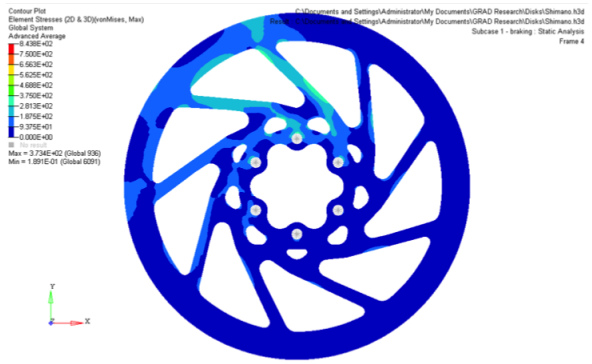

(b)

Figure C.1: Von Mises stress distribution comparison between equivalent point (a) and distributed (b) loads on a Shimano rotor.

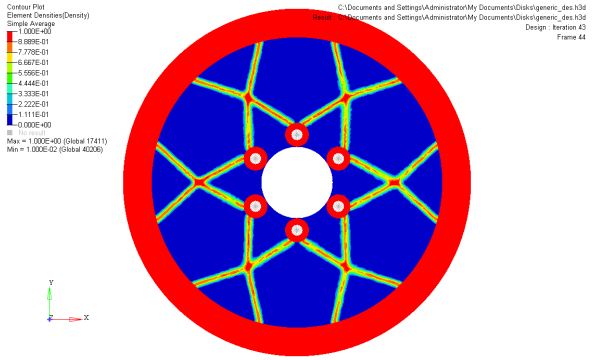

(a) Load Case 1: Aligned with bolt holes.

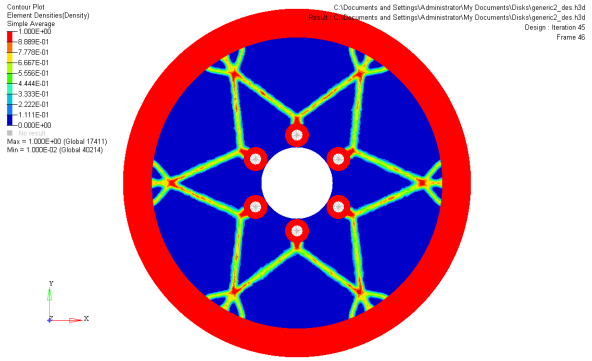

(b) Load Case 2: Unaligned with bolt holes.

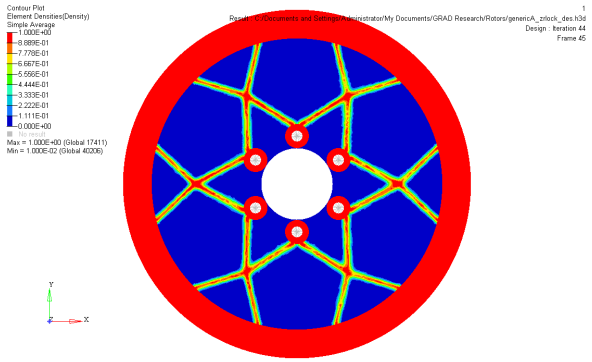

(c) Load Case 1 and 2

Figure C.2: Load cases considered individually versus simultaneously during optimization. Note that the intersection of beams that make the "X" structure is closer to the circumference of the rotor in (c) than in (a).

Appendix D

Unsatisfactory Rotor Designs

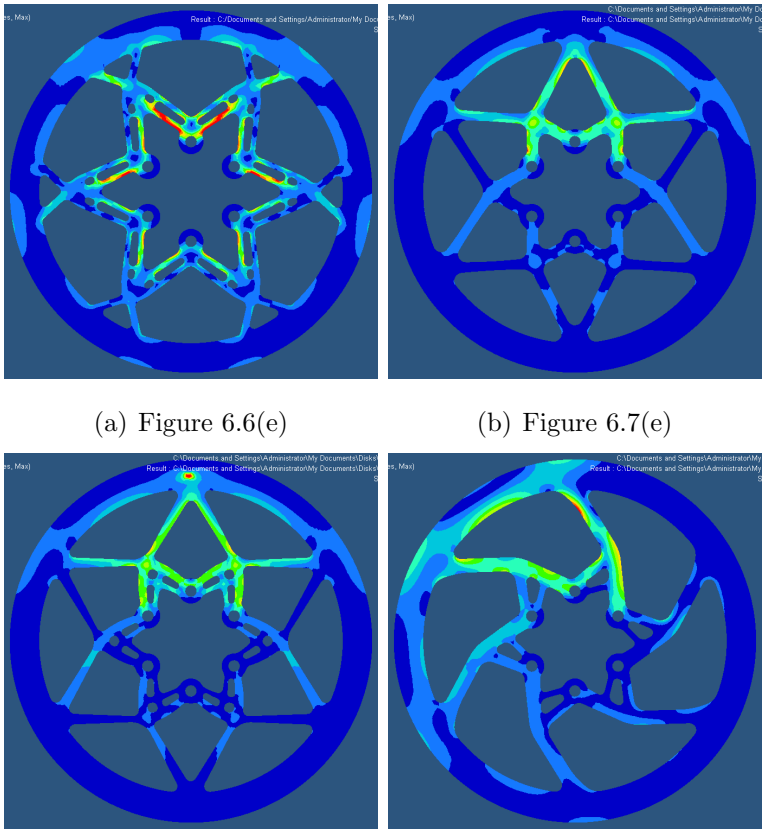

(a) Figure 6.6(e)

(b) Figure 6.7(e)

(c) Figure 6.5(e)

(d) Figure 6.2(c)

Figure D.1: Stress distribution of failed designs under the rotating screw BC, based on various optimization solutions shown in stated figures.

Appendix E

Select Iterations During Optimization

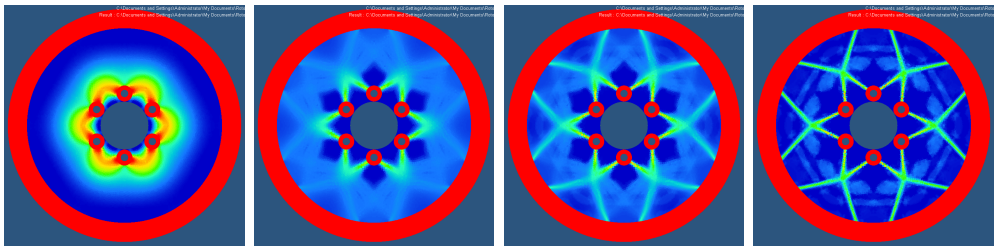

(a) Iteration 2 of 47 (b) Iteration 18 of 47 (c) Iteration 21 of 47 (d) Iteration 25 of 47

Figure E.1: Iterations of an optimization problem leading to an "X" pattern solution.

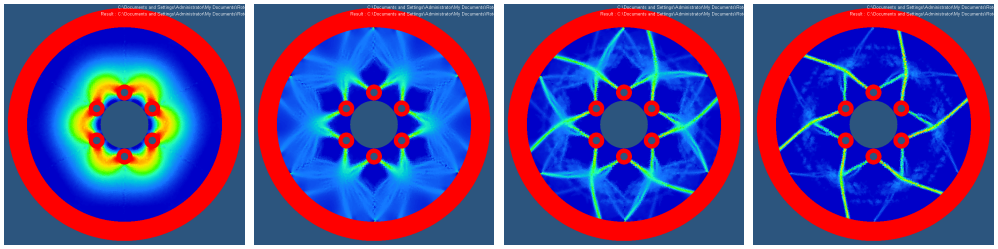

(a) Iteration 2 of 50 (b) Iteration 21 of 50 (c) Iteration 26 of 50 (d) Iteration 30 of 50

Figure E.2: Iterations of an optimization problem leading to a "tiller" pattern solution.

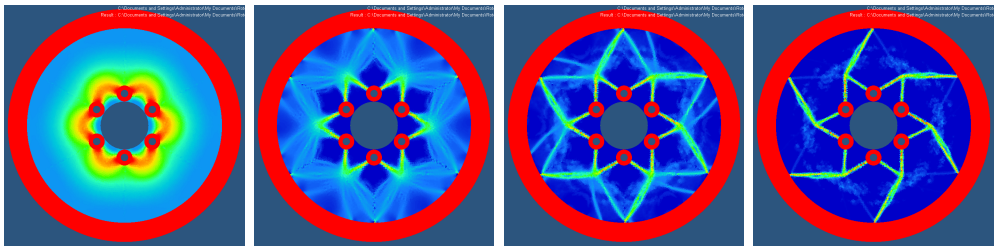

(a) Iteration 2 of 48 (b) Iteration 21 of 48 (c) Iteration 25 of 48 (d) Iteration 29 of 48

Figure E.3: Iterations of an optimization problem leading to a reverse "tiller" pattern solution.

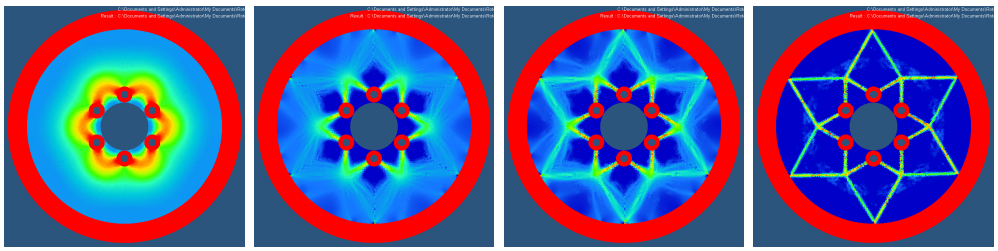

(a) Iteration 2 of 48 (b) Iteration 19 of 48 (c) Iteration 22 of 48 (d) Iteration 30 of 48

Figure E.4: Iterations of an optimization problem leading to a "star" pattern solution.

Appendix F

Buckling Mode Shapes

See Table 7.2 for buckling factors to corresponding figures below. Mode shapes shown are from buckling result under Load Case 1 orientation only (see Figure 5.3.

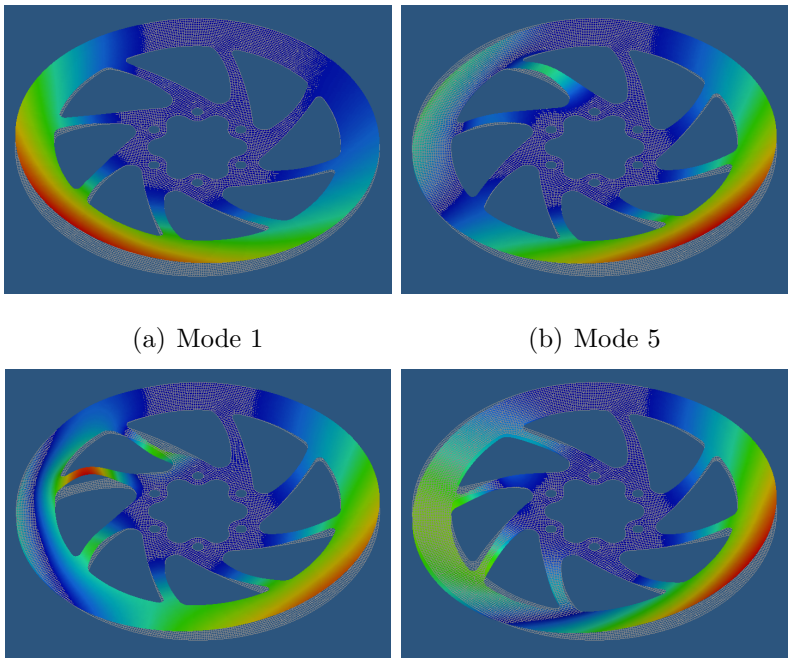

(a) Mode 1 (b) Mode 5

(c) Mode 7 (d) Mode 9

Figure F.1: Buckling mode shapes for the Hayes rotor under recommended loading direction.

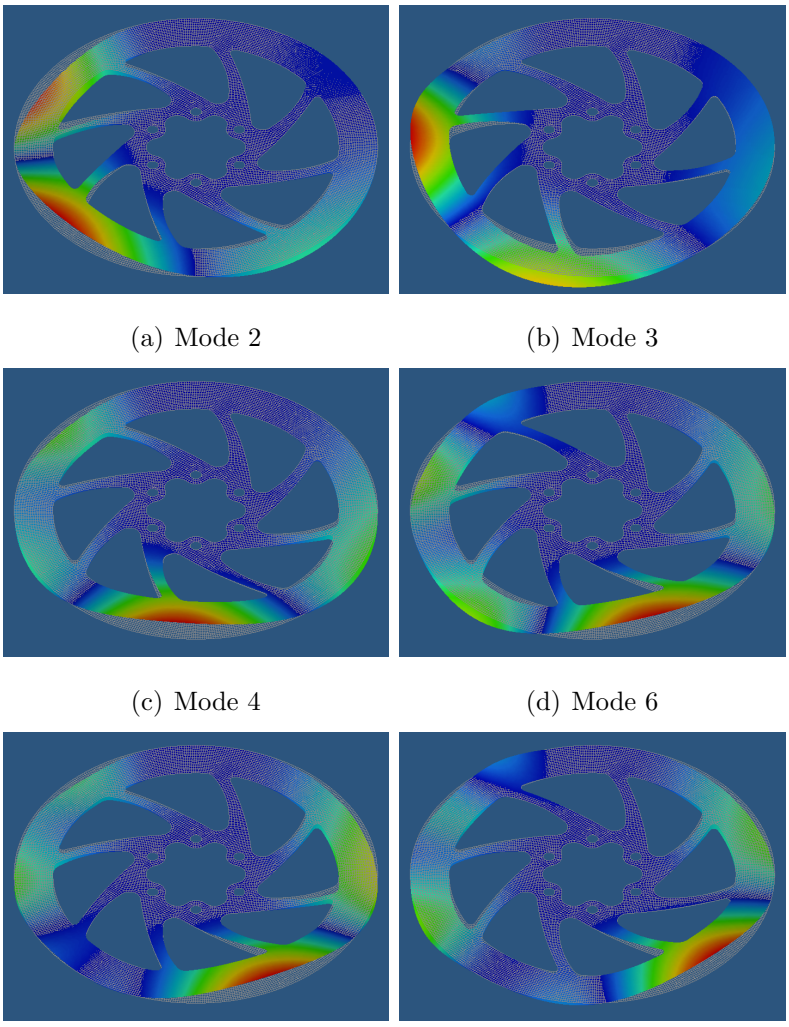

(a) Mode 2 (b) Mode 3

(c) Mode 4 (d) Mode 6

(e) Mode 8 (f) Mode 10

Figure F.2: Buckling mode shapes for the Hayes rotor under reverse loading direction.

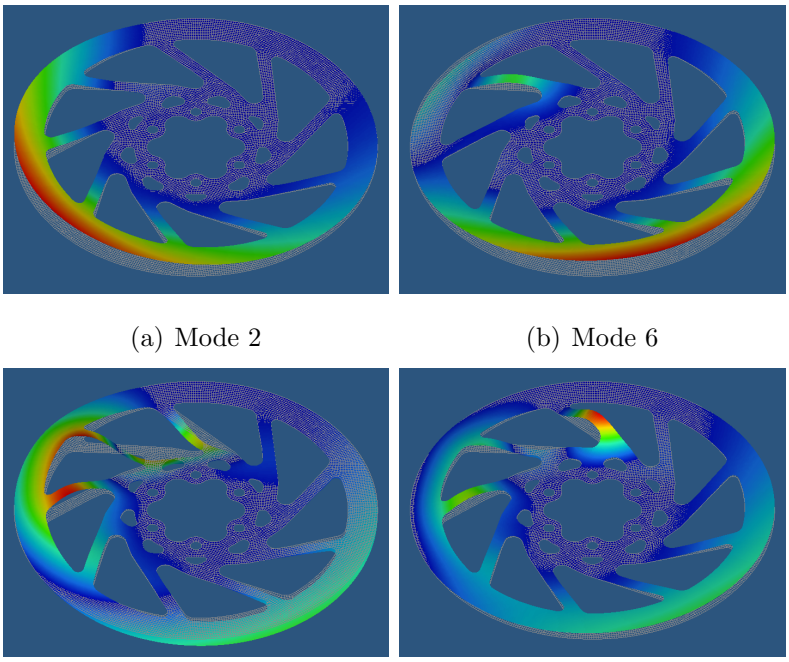

(a) Mode 2 (b) Mode 6

(c) Mode 7 (d) Mode 9

Figure F.3: Buckling mode shapes for the Hayes rotor under recommended loading direction.

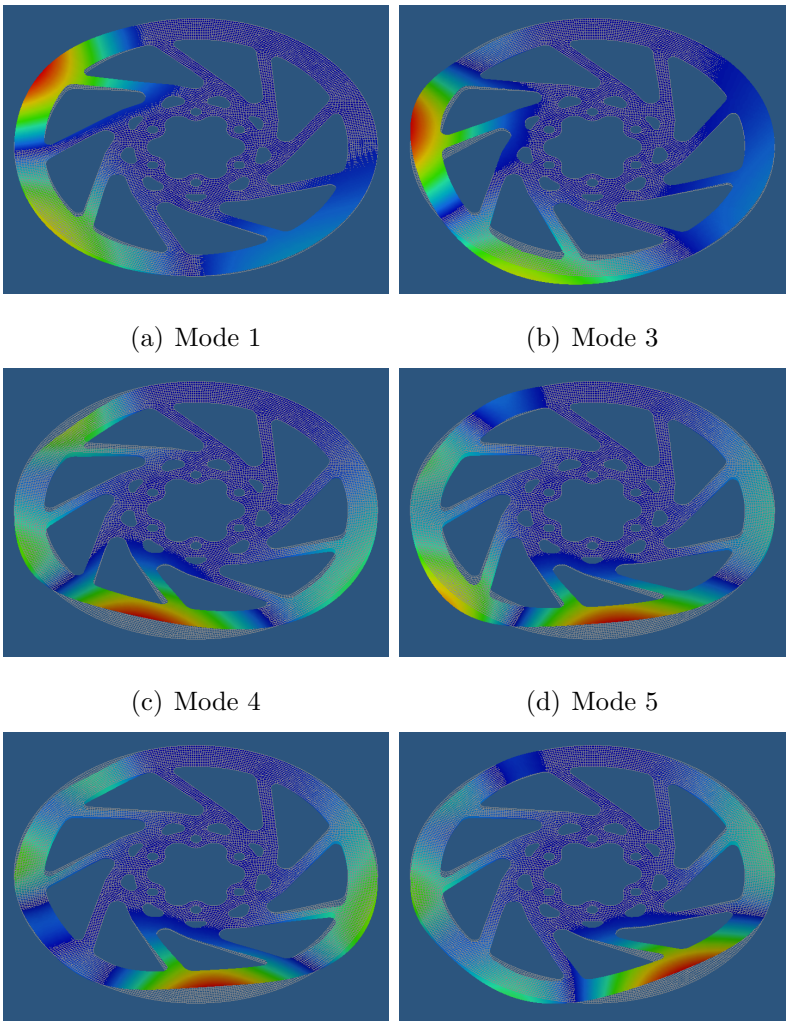

(a) Mode 1 (b) Mode 3

(c) Mode 4 (d) Mode 5

(e) Mode 8 (f) Mode 10

Figure F.4: Buckling mode shapes for the Shimano rotor under reverse loading direction.

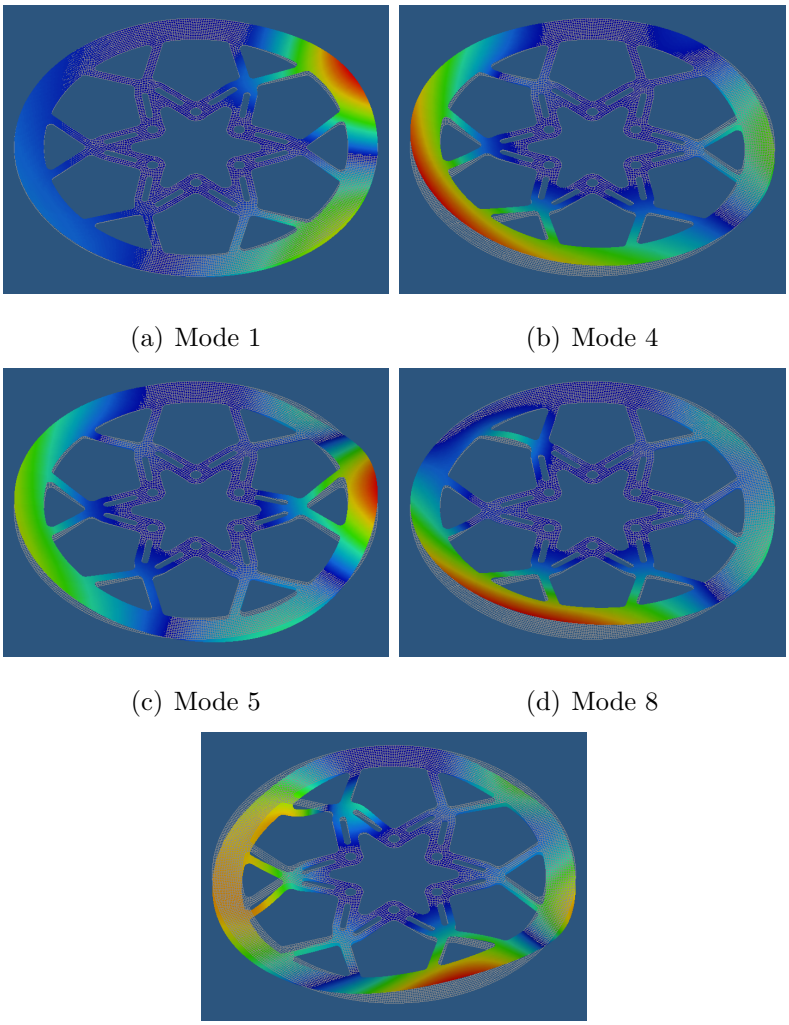

(a) Mode 1

(b) Mode 4

(c) Mode 5

(d) Mode 8

(e) Mode 10

Figure F.5: Buckling mode shapes for the new rotor under recommended loading direction.

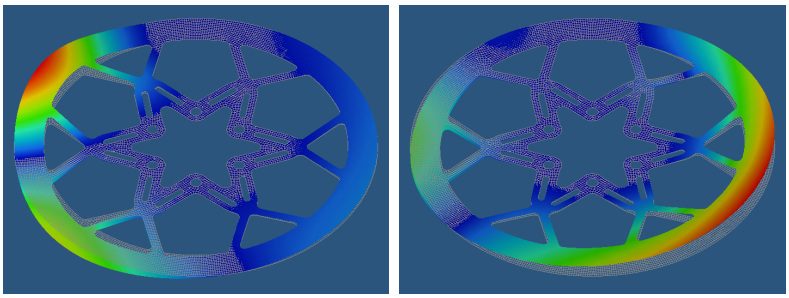

(a) Mode 2

(b) Mode 3

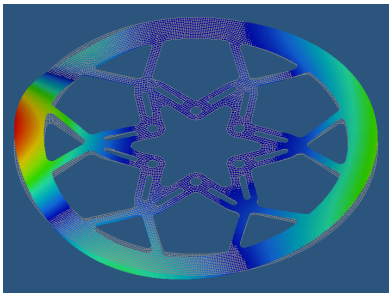

(c) Mode 6

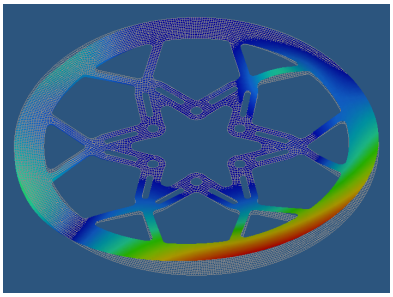

(d) Mode 7

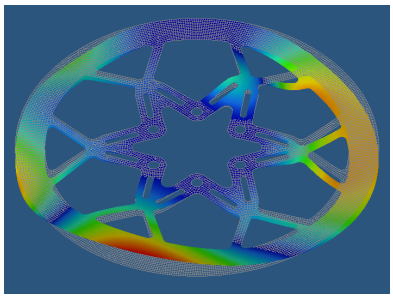

(e) Mode 9

Figure F.6: Buckling mode shapes for the new rotor under reverse loading direction.

Appendix G

Supplemental Rotor Symmetrical Instance Analysis

Additional investigations on whether similar results in design would occur for different number of optimization cyclic symmetry constraint instances. It is seen in Figure G.1 that the same design types of "tiller", "X", and "star" exist, but with different number of arms depending on the number of symmetric instances. In some cases, the number of symmetric instances chosen do not create any real rotor symmetry with the six hole mounting pattern. This makes it difficult to choose where to put the loads acting on the rotor. Figure G.2 shows the result of using a load case at each point of mounting hole symmetry, using a load case at each optimization constraint symmetry, and using a load case at each optimization constraint symmetry for half the disc to account for the non-symmetric nature of the disc when considering both symmetries (Figures G.2(a), G.2(b), G.2(c), respectively). Figure G.2 also shows that even for non-symmetric rotors, a tiller type design is a possibility for a feasible rotor design.

It can also be observed that better, or more well defined, solutions are given for some cases. The solutions for 5, 7 and 8 optimization symmetry constraint instances (Figures G.1(b), G.1(d), and G.1(e), respectively) give thickness to elements that serve no structural purpose. Although feasible designs for any number of symmetrical instances may exist, these solutions suggest that using the

true rotor symmetry of 6 instances give the best possibility for an optimal design.

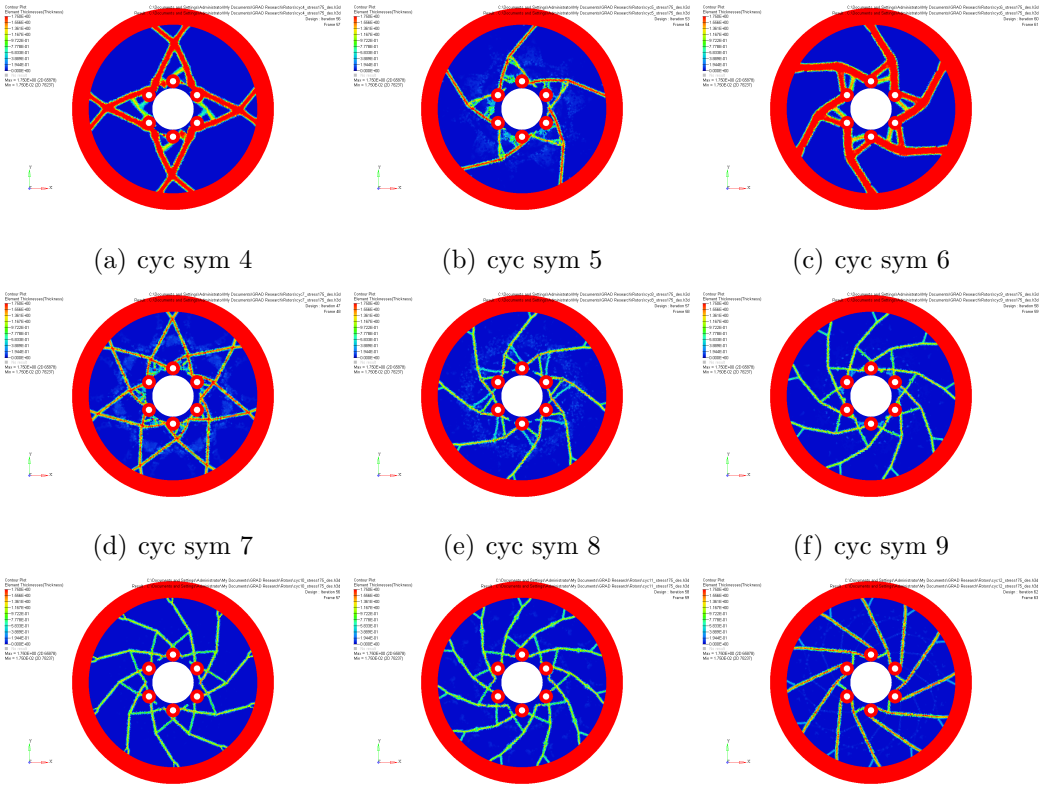

(a) cyc sym 4 (b) cyc sym 5 (c) cyc sym 6

(d) cyc sym 7 (e) cyc sym 8 (f) cyc sym 9

(g) cyc sym 10 (h) cyc sym 11 (i) cyc sym 12

Figure G.1: Optimization result under various cyclic symmetry constraints.

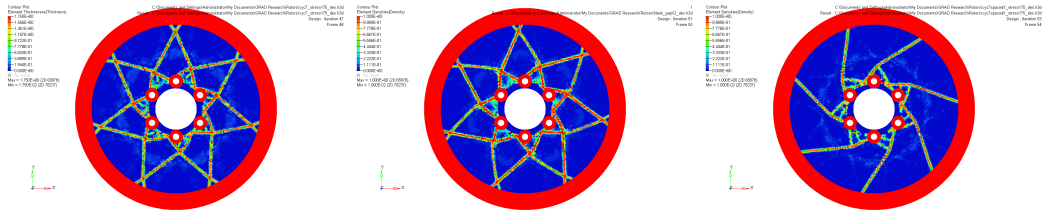

(a) loads at 0 and 330 deg (b) loads at 0 and 334.286 deg (c) loads at 0 and every $\frac{360}{14}$ deg CCW for 8 reps

Figure G.2: Optimization result under 7 part cyclical symmetry constraint with various tangential loads at the same radial distance.

Bibliography

[1] B. Breuer and K. H. Bill, eds., *Brake Technology Handbook*. Warrendale, PA: SAE International, 1st english ed., 2008.

[2] Altair Engineering, Inc., *RADIOSS, MotionSolve, and OptiStruct*, 2008.

[3] H. Zhu and D. B. Bogy, "DIRECT Algorithm and Its Application to Slider Air-Bearing Surface Optimization," *IEEE Transactions on Magnetics*, vol. 38, pp. 2168–2170, Sep 2002.

[4] <http://www.gelioscope.com/?tag=/saddle>, 2009. Website.

[5] S. Griffith, "Mountain Biking Before Mountain Bikes." <http://www.rsf.org.uk/history.htm>, 2009. Online posting.

[6] "Marin Story." <http://www.marinbikes.com/2010/bike_pages.php?page=About-Marin_Marin-Story>, 2009. Online posting.

[7] <http://www.interbike.com>, 2010. Website.

[8] <http://www.seaotterclassic.com/index.cfm/trade_show_expo_attendees.htm>, 2010. Website.

[9] "Requirements for Braking System." Code of Federal Regulations. Title 16 Part 1512.

[10] G. R. Watts, "Brakes on Pedal Cycles," in *Braking of Road Vehicles: I Mech E Conference Publications 1983-2*, (London), pp. 25–28, The Automobile Division of The Institution of Mechanical Engineers, Mechanical Engineering Publications Limited for the Institution of Mechanical Engineers, 1983.

[11] F. R. Whitt and D. G. Wilson, *Bicycling Science*. Massachusetts Institute of Technology, 2nd ed., 1982. ISBN 0-262-23111-5.

[12] T. J. R. Hughes, *The Finite Element Method*. Mineola, NY: Dover Publications, 2000. ISBN 0-486-41181-8.

[13] P. Kinney, "Cleanup: Improving Quadrilateral Finite Element Meshes," tech. rep., Ford Motor Company, Dearborn, MI, Feb 2008.

[14] F. E. Talke. Class Lecture, 2008. Computer-Aided Design and Analysis.

[15] P. Sergeant, I. Cimrák, V. Melicher, L. Dupré, and R. V. Keer, "Adjoint Variable Method for the Study of Combined Active and passive Magnetic Shielding," *Mathematical Problems in Engineering*, vol. 2008, 2008.

[16] J. R. Shewchuk, "An Introduction to the Conjugate Gradient Method Without the Agonizing Pain," tech. rep., School of Computer Science, Carnegie Mellon University, Pittsburg, PA, Aug 1994.

[17] C. L. Odgen, C. D. Fryar, M. D. Carroll, and K. M. Flegal, "Mean Body Weight, Height, and Body Mass Index, United States 1960-2002," tech. rep., U.S. Depertment of Health and Human Services, Oct 2004.

[18] M. Hermanussen, H. Danker-Hopfe, and G. W. Weber, "Body Weight and the Shape of the Natural Distribution of Weight, in Very Large Samples of German, Austrian and Norwegian Conscripts," *International Journal of Obesity*, vol. 25, pp. 1550–1553, 2001.

[19] J. L. Meriam and L. G. Kraige, *Engineering Mechanics*, vol. 2 Dynamics. Hobokan, NJ: John Wiley and Sons, Inc., 5th ed., 2002. ISBN 0-471-40645-7.

[20] F. P. Beer, E. R. Johnston, E. R. Eisenberg, and W. E. Clausen, *Vector Mechanics for Engineers: Statics and Dynamics*. New York, NY: McGraw-Hill, 7th ed., 2004. ISBN 0-07-230491-X.

[21] "Friction and Coefficients of Friction." <http://www.engineeringtoolbox.com/friction-coefficients-d_778.html>, 2010. Webpage.

[22] "Hayes "U"." <http://www.hayesdiscbrake.com/hayesu_product1.shtml>, 2009. Webpage.

[23] Altair Engineering, Inc., *HyperMesh and BatchMesher*, 2008.

[24] "Stainless Steel for a Disc Brake Rotor." United States Patent 6386342 B1.

[25] "AISI Type 403." <http://www.efunda.com/Materials/alloys/stainless_steels/show_stainless.cfm?ID=AISI_Type_403&show_prop=all&Page_Title=AISI%20Type%20403>, 2010. Webpage.

[26] "Seasons Sponsors." <http://www.thecollectivefilm.com/seasons>, 2008. Webpage.

[27] "A Successful Sea Otter for the Hayes Bicycle Group." <http://www.hayesdiscbrake.com/news_latest.shtml>, 2008. Online posting.

[28] D. R. Askeland and P. P. Phulé, *The Science and Engineering of Materials*. Pacific Grove, CA: Brooks/Cole-Thomson Learning, 4th ed., 2003. ISBN 0-534-95373-5.

[29] <http://www.ashima.com.tw/products_01_01.html>, 2010. Webpage.

[30] <http://formulabrakeusa.com/07-collection/rx/>, 2010. Webpage.

[31] <http://www.sram.com/en/avid/>, 2010. Webpage.

[32] <http://www.magura.com/en/home.html>, 2010. Webpage.

[33] "Shimano Technical Documents." <http://techdocs.shimano.com/techdocs/index.jsp>, 2010. Webpage.

[34] <http://www.hayesdiscbrake.com/product_af_discrotors.shtml>, 2010. Webpage.

[35] "Dirty Dog Mtb Skull Stem, Cable Ties and Brake Rotors." <http://www.bikerumor.com/2009/04/28/

dirty-dog-mtb-skull-stem-cable-ties-and-brake-rotors/>, 2009. Online Posting.

[36] <http://www.hopetechusa.com/>, 2010. Webpage.

[37] <http://www.cyclebrakes.com/html/our_products.html>, 2010. Webpage.

[38] <http://www.brembo.com/US/Motorsports/>, 2010. Webpage.

[39] <http://www.superstreetbike.com/hotproducts/0809_sbkp_cts_moto_brake_rotor/photo_01.html>, 2010. Webpage.

[40] W. T. Thomson and M. D. Dahleh, *Theory of Vibration with Applications*. Upper Saddle River, NJ: Prentice-Hill, 5th ed., 1998. ISBN 0-13-651068-X.